Electrochimica Acta 368 (2021) 137642

Contents lists available at ScienceDirect

Electrochimica Acta

journal homepage: www.elsevier.com/locate/electacta

Development of Co/Co_9S_8 metallic nanowire anchored on N-doped CNTs through the pyrolysis of melamine for overall water splitting

Anchu Ashok[a], Anand Kumar[a,*], Janarthanan Ponraj[b], Said A Mansour[b]

[a] Department of Chemical Engineering, College of Engineering, Qatar University, P O Box – 2713, Doha, Qatar
[b] Qatar Environment and Energy Research Institute (QEERI), Hamad Bin Khalifa University, Qatar Foundation, PO Box 34110, Doha, Qatar

ARTICLE INFO

Article history:
Received 16 September 2020
Revised 13 December 2020
Accepted 13 December 2020
Available online 21 December 2020

Keywords:
Oxygen evolution reaction (OER)
Hydrogen evolution reaction (HER)
Overall water splitting
Melamine pyrolysis
MWCNT catalysts

ABSTRACT

Herein, we report the successful synthesis of Co_9S_8 metal-sulfide nanowire trapped in multi walled carbon nanotube (MWCNT), which was subsequently found to be an effective catalyst for water splitting. Melamine pyrolysis together with a Co precursor results in MWCNTs, with the addition of sulfur during synthesis enhancing the surface area, pore size, and oxygen vacancy defects in the nanotubes. The hierarchical structure of Co/Co_9S_8/CNT products boosted the electron mobility and mass transport for both the oxygen evolution (OER) and hydrogen evolution reaction (HER) in alkaline medium. Doping the catalyst surface with Pyridinic-N atoms, Graphitic-N atoms and thioamide S-atoms dramatically improved the bifunctional electrocatalytic performance by lowering the overpotentials for OER and HER reactions. The Co/Co_9S_8/CNT generated a current density of 10 $mAcm^{-2}$ water-splitting current by applying a cell voltage of only 1.5 V. Further, Co/Co_9S_8/CNT showed excellent stability. The mechanism of Co_8S_9 nanowire formation in the MWCNT was also investigated.

1. Introduction

Current worldwide demand to reduce the usage of unsustainable fossil fuels to overcome the alarming rise in global warming gained a wide scientific attention to look for cleaner alternatives. A diversion to cleaner energy forms offers long term advantages that are not possible with the conventional energy sources such as coal, oil, and gas. In the last decade, many studies has been conducted to develop new energy storage systems and conversion technologies such as fuel cells, metal air batteries and water splitting devices [1–8]. The activity and efficiency of the chemical transformation on these renewable devices are governed by the electrocatalyst driving the conversion reaction. Electrochemical water splitting involves two-cell reactions; hydrogen evolution reaction (HER) and oxygen evolution reaction (OER) as a reliable pathway for the generation of hydrogen and oxygen, respectively. Both the reactions require an overall thermodynamic potential of minimum 1.23 V to proceed with a successful overall water splitting. However, practically, the kinetic hindrance requires extra potential to drive the reaction and the over-all system becomes costlier limiting its practical application [9–14]. It is highly recommended to develop outstanding electrocatalysts to overcome the current sluggish kinetics without compromising the stability.

The state-of-the-art shows Ir, Ru and their derivatives offering good activity for OER and Pt based material exhibiting the most active performance for HER; however their scarcity, high cost and severe operating condition hamper the commercial application in large scale [15–23]. Transition metal based electrocatalysts gained research attention owing to the low cost and large-scale availability. Numerous studies have been devoted on transition metal alloys, oxides, and carbides as bifunctional electrocatalysts [24–35]. Nevertheless, the transition-metal catalysts alone suffer from intrinsically low electron conductivity limiting their performance towards high current densities. To overcome this, some conductive materials such as carbon nanomaterials, graphene layers or carbon nanotubes (CNTs) are commonly employed as effective supports for the transition metal catalyst. Even though, these carbonaceous materials alone are not known to have high activity for most of the electrochemical reactions, their electrochemical performance can be further improved by doping some heteroatoms such as boron, nitrogen or phosphorous [31,32]. These carbonaceous materials can act either as an active metal-free electrocatalyst or as an efficient catalyst support for the active metal nanoparticles that generate synergistic catalytic activity. Among the different types of heteroatoms being used, nitrogen gained a great attention due to the low cost, durability and unique structure. The electronic and

* Corresponding author.
E-mail addresses: akumar@qu.edu.qa, akumar1@alumni.nd.edu (A. Kumar).

https://doi.org/10.1016/j.electacta.2020.137642

chemical properties of N-doped CNTs significantly changes the induced property of the asymmetric spin density and local charge density of the carbon lattices, thereby altering the reaction route resulting in an improved surface chemical reactivity of HER and OER mechanism [36]. Various studies show that pyridinic nitrogen serves as a promising active site for OER and ab initio calculations proved that N doped CNTs increases the Fermi Level at donor state to facilitate the emission of large current at lower applied voltage [37,38].

Recently, transition metal sulfides are found to be highly tolerable to oxidation environment than transition metal alloys, phosphides, and nitrides [39]. Metal sulfides demonstrated prominent electrochemical properties due to their unique physio-chemical properties such as thermal and electrical conductivity, mechanical and thermal stability. Cobalt sulfides (Co_3S_4, CoS_2, Co_9S_8, $Co_{1-x}S$) show a great potential in hydrogen and oxygen electrocatalysis applications [40–43]. Particularly, Co_9S_8 is found to be as a promising electrocatalyst with exceptional properties in the microchemical interface of the catalysts due to its good durability and outstanding redox capability in alkaline medium. The electrochemical activity of Co_9S_8 can be improved through proper doping, tuning morphology, incorporating functional materials or substrates. Anchoring Co_9S_8 over doped CNTs plays a synergistic effect to improve the overall electron conductivity, which enhances the electrocatalytic properties [44,45].

Liu and coworkers synthesized hierarchical Co_9S_8 hollow microplates using sulfurization and calcination process that exhibits remarkable performance for oxygen evolution reaction with low over potential (278 mV) to reach 10 $mAcm^{-2}$ with low Tafel slope (53 $mVdec^{-1}$) and excellent stability [46]. Nanda and team, followed a green and environment-friendly pyrolysis method for the successful synthesis of metal-rich sulfide anchored over N-doped nanocarbon network in absence of S^{2-} ions that show excellent OER activity when compared to commercial RuO_2 [47]. Yuan et al. fabricated Co@Co_9S_8 nanochain with core-shell morphology using direct-current arc-discharge technique followed by sulfurization at 200 °C. The Co nanochain acts as a conductive network that injects electron to Co_9S_8 and enhances the OER performance significantly by reducing the overpotential for oxygen evolution reaction [48]. Feng and co-workers prepared carbon armored Co_9S_8 nanoparticles through the direct thermal treatment of cobalt nitrate and trithiocyanuric acid mixture heated upto 700 °C under N_2 flow. The Co_9S_8@C exhibits excellent HER activity and durability over both extreme condition of acidic and basic medium with 100% faradaic efficiency for hydrogen evolution [49]. Zhuo and coworkers reported the preparation of Co_9S_8 using electrochemical deposition technique and its incorporation with MoS_x using single step sulfurization method. They studied the effect of small amount of MoS_x on the electrocatalyst HER activity of Co_9S_8. Moreover, Co_9S_8–30@MoS_x/CC was found to be the excellent catalyst towards HER with a low overpotential of −98 mV at 10 $mAcm^{-2}$ along with a low Tafel slope and outstanding stability [50]. Li et al. designed Co_9S_8/CNFs membrane by combining electrospinning and chemical vapor deposition that shows excellent activity and stability for HER/OER. The onion like graphene layer wrapped around the nanoparticles not only enhances the electrical conductivity but also prevent the degradation of particle during electrocatalysis and thereby enhances the stability [51]. Liu and researchers synthesized Co_9S_8@N,P-doped porous carbon (Co_9S_8@NPC) using low-temperature phosphorization method with Co_9S_8@N-doped porous carbon as a precursor that was prepared using a one-step molten-salt calcination method. Co_9S_8@NPC displays good activity towards OER/HER and was used simultaneously for cathode and anode catalyst for the generation of hydrogen and oxygen with 100% faradaic efficiency [52]. Inspired by the above observation, our aim is to develop ultrafast, economical, and scalable method for the synthesis of Co_8S_9 anchored over carbon network that would enhance the electronic conductivity. There are some reports available in literature on the N-doped CNTs embedded with transition metal nano-catalyst that show high electrocatalytic activity [44,45]. In this work we focus on the mechanism of formation of Co_9S_8 metal-sulfide nanowire trapped in multi walled carbon nanotube (MWCNT) and compare its intrinsic effect towards electrocatalytic activity with respect to Co based catalyst without sulfur doping.

In this work we followed melamine assisted pyrolysis in presence of metal salt for the synthesis nanoparticles incorporated N-doped CNTs and investigate their electrochemical property for HER, OER and overall water splitting. Melamine was not only the source of carbon but also provided N atoms for doping over the graphene network. Furthermore, the mechanism of CNT formation in presence of Co nanoparticle is also proposed on the basis of the characterization as well as from previous reports.

2. Experimental procedure

2.1. Synthesis method

Cobalt nitrate (0.5 g, 99.9%, Sigma Aldrich), melamine (4 g, 99%, Sigma Aldrich), thioamide (1 g, ≥ 99.0%, Sigma Aldrich) and ethanol was provided by BDH Middle East LLC. All reagents were used as received without any further step of purification. A 0.5 g of cobalt nitrate and 4 g of melamine and 1 g of thioamide was uniformly mixed using a hand motor for 10–15 min. The mixture was loaded in a quartz boat and placed inside a horizontal calcination furnace for pyrolysis at 900 °C for 2 h at a ramp of 4 °C/min under continuous N_2 flow (10 sccm). The obtained sample was alternately washed with DI water, ethanol and acetone to remove undue metal and unwanted elements. The washed sample was then filtered and dried under vacuum at 80 °C for overnight. Thus obtained final product was names as Co/Co_9S_8/CNT. Another sample, Co/CNT without sulfur, was also prepared for electrochemical activity comparison.

2.2. Material characterization

Crystalline nature of the synthesized particles were measured using PANanalytical (Empyrean) with a scan range of 10–90° with a step size of 0.013° at 0.154056 nm wavelength of Cu-Kα radiation. Crystal structure of synthesized particle was modeled using VESTA software package. Diffraction peaks were analyzed and identified using HighScore Plus coupled with the XRD equipment. AimSizer (AS-3012) BET area analyzer was used to identify the surface area, pore size and pore volume of the synthesized catalysts. Nova Nano 450, FEI, Scanning Electron Microscope (SEM) with magnification up to 200 kx along with EDX was used to identify the morphology and elemental composition. Transmission Electron Microscopy (TEM, FEI Talos F200X) coupled with FEI SuperX EDS system was used to identify the particle size, structure, and phase composition. Kratos AXIS Ultra DLD, X-Ray Photoelectron Spectroscopy (XPS) was used to identify the bonding configuration, elemental composition and their oxidation states. Raman spectrometer (DXR Thermoscientific) was used for the detailed analysis of carbon formed within the range of 10 cm^{-1} to 4000 cm^{-1} with the step size of 1.5 cm^{-1} and step time of 20 s at a wavelength of 514.53 nm.

2.3. Electrochemical measurement

HER and OER analysis was conducted with PINE instrument bipotentiostat (Wave Driver 20) on a 3-cell electrode system in 1 M KOH alkaline electrolyte at room temperature. The electrode system consists of a 5 mm glassy carbon disk supported over Teflon mounting as a working electrode, Pt coil (99.9%) mounted at the

end of a chemically resistant epoxy rod as counter electrode and Ag/AgCl (4 M saturated KCl) as a reference electrode. Typically the procedure for preparing working electrode is as follows: A 5 mg of catalyst and a 30 µL Nafion (0.125% as a binder) was mixed well with a 300 µL of isopropyl alcohol followed by 30 min sonication. A 5 µL of the catalyst ink was dropped slowly over the glassy carbon disk and allowed to dry it at room temperature. The Nernst equation ($E_{RHE} = E_{Ag/AgCl} + 0.197 + 0.0591 \times pH$) was used to convert all potential reported into standard reversible hydrogen electrode (RHE). Prior to the experiment, a 120 mL of 1 M KOH was completely purged with N_2 (20 sccm) in order to remove the unwanted contaminants. The working electrode was electrochemically pretreated with 100 reduction/oxidation cycle between 0.4 to −1 V at a scan rate of 500 mVs^{-1} to make the catalyst surface stable. The electrocatalytic activity of the catalysts was measured using Cyclic Voltammogram (CV), Linear Sweep Voltammetry (LSV) and Chronoamperometry (CA).

The Faradaic efficiency of the electrocatalyst for OER was obtained using a rotating ring disk electrode (RRDE) setup, where the catalyst loaded on the central disk electrode generates oxygen (as a result of oxygen evolution reaction) and the surrounding Pt ring electrode maintained at a fixed potential (ORR potential) collects the generated oxygen and reduces it (oxygen reduction potential). A 1 M KOH solution was purged with N_2 for 30 min to get rid of any dissolved oxygen prior to the experiments. The disk electrode was scanned between 1.5 to 1.6 V vs RHE with an electrode rotation of 1600 rpm, while the Pt ring electrode was held at a constant potential of 0.4 V RHE in order to rapidly reduce the oxygen evolved from the disk. The faradaic efficiency can be calculated using the equation;

$$FE(\%) = \frac{2I_r}{NI_d} \quad (1)$$

Where I_r and I_d are the measured ring and disk currents respectively, and N denotes the collection efficiency (taken as 0.24 here) [53–55]. The value 2 denotes the apparent number of electrons and be reported as 2 for electrode at 1600 rpm. Moreover, the RRDE measurement helps to identify the mechanistic pathway for oxygen evolution reaction by fixing the potential of ring at 1.4 V and measuring the current at ring disk to detect the presence of H_2O_2 oxidation.

Zahner Elektrik IM6 was used to measure the electrochemical impedance analysis at different potentials with frequencies ranging from 0.1 Hz to 100 kHz with an amplitude of 5 mV. The impedance components were extracted using Thales, Equivalent Circuit Simulation & Model Fit (SIM).

The overall water splitting was conducted in a two-electrode system with anode and cathode as Co/CNT (or Co/Co_9S_8/CNT) catalyst. The electrode was fabricated using carbon cloth (1 cm x 3 cm) pretreated twice using HNO_3 (0.1 M), ethanol (0.1 M) and DI water alternately. Typically, a 3 mg of catalyst was dispersed in a mixture of DI water (1 mL), isopropyl alcohol (0.5 mL) and Nafion solution (0.03 mL) by sonication for 30 min. A 35 µL of thus prepared ink was dropped carefully on both the side of 1 cm x 1 cm portion of carbon cloth and allowed to dry in an oven kept at 40 °C. The prepared electrode was used in a two-cell electrode system to perform the polarization curve measurement in N_2 saturated 1 M KOH electrolyte.

3. Result and discussion

XRD patterns for Co/CNT and Co/Co_9S_8/CNT are shown in Fig. 1a. In Co/CNT pattern, the peaks at 2θ = 44.23°, 51.23° and 75.8° can be attributed to the (111), (200) and (220) planes of cubic (F m −3 m) metallic Co. The XRD pattern of Co/Co_9S_8/CNT, with the peaks at 2θ= 15.45°, 29.8°, 31.1°, 37.03°, 39.5°, 47.56°, 52.06°, 73.2° and 76.7° confirm the successful formation Co_9S_8 along with metallic Co. The strong peak at 2θ=26.05° corresponds to the (002) plane of graphene layer, which is present in both Co/CNT and Co/Co_9S_8/CNT confirming the formation of CNTs during the pyrolysis of melamine. The possibility of metal-carbide formation is there, as the peak at 44.2° corresponds to Co_3C and 44.6° belongs to metallic Co. A prospect of overlapping of these peaks exists and an XPS analysis will be used to further confirm the existence of metal-carbide on the surface [56]. Crystal structures of Co and Co_9S_8 in Co/CNT and Co/Co_9S_8/CNT respectively confirm a cubic crystal structure with Fm3m space group in both catalysts, where the unit cell parameter of Co/Co_9S_8/CNT and Co/CNT were calculated to be 978.56 Å and 44.7 Å respectively. The presence of sulfur during synthesis increase the cubic volume by approximately 144% than the initial value. N_2 adsorption-desorption isotherm method (Figure S1.a) was used to calculate the specific surface area, pore size and pore volume of as-synthesized particles. The Brunauer–Emmett–Teller (BET) specific surface area of Co/CNT and Co/Co_9S_8/CNT was measured to be 65.7 $m^2\ g^{-1}$ and 78.2 $m^2\ g^{-1}$, respectively. A distribution of pore size and pore volume obtained from BJH (Barrett-Joyner-Halenda) method in Figure S1.b shows an average pore radius of 1.9 nm and 1.94 nm respectively for Co/CNT and Co/Co_9S_8/CNT. The pore volume of Co/CNT was measured to be 0.346340 cc/g, while that of Co/Co_9S_8/CNT was 0.475201 cc/g. The significant increase in the surface area and pore volume in Co/Co_9S_8/CNT sample is possibly due to the doping of sulfur. The larger specific surface area provides an easier pathway for rapid movement of ions and electrons during catalytic reactions. Moreover, the larger pore volume facilitates a faster diffusion through the sufficient contact of electrolyte to the active surface area and thereby increases the specific capacity and overall electrochemical performance. The morphology of as-prepared Co/CNT and Co/Co_9S_8/CNT samples in Figure S2(a-b) confirm the presence of carbon nanotubes of several nanometer to micrometer length where the metal nanoparticles are encapsulated at the end (bright contrast). The diameter of the carbon nanotubes are similar to that of the particle size, which are in the range of 10 to 25 nm. EDX analysis in Figure S2(c-d) confirm the presence of Co, C, O and N in Co/CNT, and the existence of S (1.35%) suggests a successful doping of S during the pyrolysis in Co/Co_9S_8/CNT. The presence of N in the elemental composition indicates the incorporation of N over the graphene lattice.

Raman spectroscopy is a powerful tool to analyses the disorderness and degree of graphitization in carbon-based samples. Figure S3 displays the Raman spectrum of as-prepared Co/CNT and Co/Co_9S_8/CNT, with two prominent peaks centered at 1358 and 1592 cm^{-1} corresponding to the D and G band of carbon respectively. The D band indicates the graphite defects such as vacancies, edge and grain boundaries, where G band corresponds to sp^2 bond of carbon. The crystallinity of the graphite plane can be quantified using the intensity ratios of D and G band centers (I_D/I_G), where the value tends to increase with an increase in the edge defect, which is associated with a decrease in the graphite size. The intensity ratio, I_D/I_G for Co/CNT and Co/Co_9S_8/CNT was calculated to be 0.75 and 0.95 respectively, suggested that the effect of sulfur doping improves the surface carbon defect that possibly enhances the microstructural surface property of the catalyst for electrochemical reactions. The weaker peaks observed around 650 cm^{-1} indicate the presence of Co (or Co_9S_8) bonded to the carbon network.

TEM/EDS analysis was used to identify the size, composition and type of carbon formed in the as-synthesized particles. TEM image of Co/CNT in Fig. 2 displays the presence of carbon nanotubes of several micrometer length with encapsulated Co nanoparticle. Mainly, the carbon formed are of a) Carbon bamboo nanotubes (CBNT), and b) multi walled carbon nanotube (MWCNT). A close observation of CBNT in Fig. 2b consists of hollow interior divided

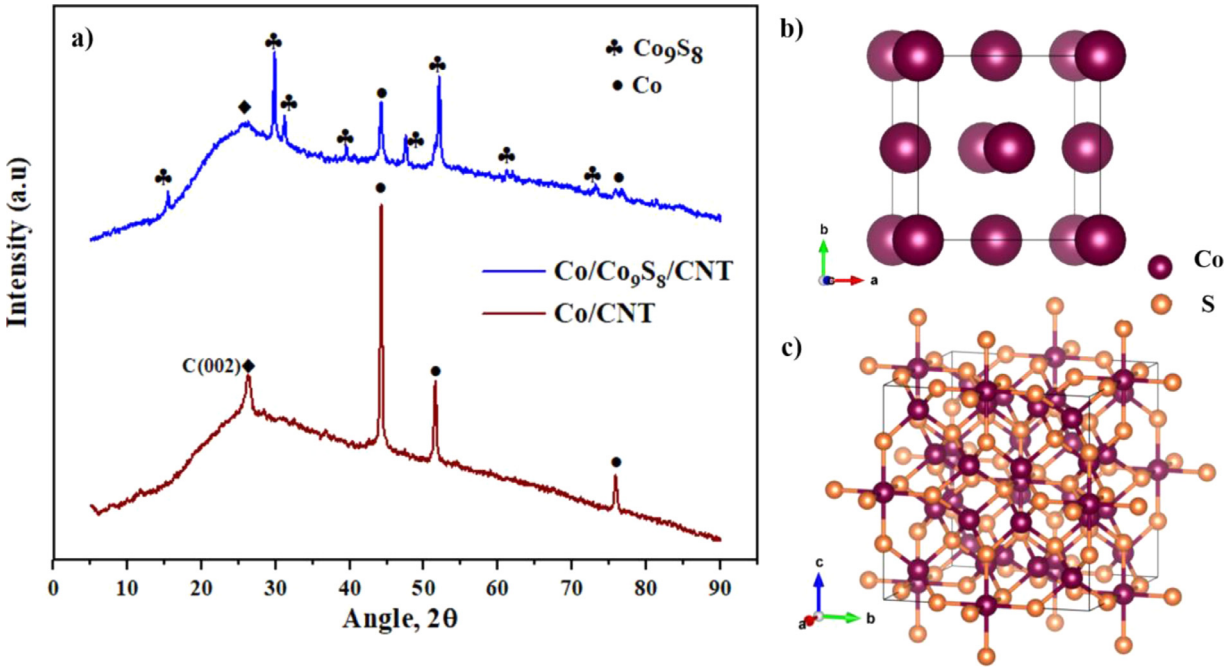

Fig. 1. (a) Powder XRD profile (b-c) crystal structure of cubic Co and cubic Co_9S_8 in Co/CNT and Co/Co_9S_8/CNT samples respectively.

into different compartments. Each compartment of 50 −100 nm size are separated with 5 −10 layers of graphene sheets, termed as graphene nodes. Co nanoparticles of 10–20 nm average size are well-dispersed in the hollow space of the CBNT, on the graphene nodes between the compartment, and on the side walls. The distribution of Co on the CBNT structure indicates a strong interaction between Co and graphene layer in CBNT. TEM image of MWCNT in Fig. 2c consist of hollow interior with 10–15 layers of graphene layers lying parallel to the tube axis. In MWCNT, each single particle in the range of 20–30 nm are trapped between the walls of the graphene layer, or at the extreme end as shown in Figure S4. The particles of semi-spherical shape are bonded with 3–5 layers of graphene sheets as shown in Figure S4. The diffraction spots in the selected area electron diffraction (SAED) pattern shown in Figure S4 inset confirm the highly crystalline nature of the particles. Moreover, it also consists of more than one diffraction pattern, which are highly likely to arise from the poorly crystallized graphene layer covering the Co nanoparticle. HAADF-STEM image and phase mapping in Fig. 2(g-i) display a uniform distribution of C and N species across the entire tubular structure, thereby confirming the successful doping of N atoms over the graphene network. Co atoms are dispersed all over the entire CBNT (Fig. 2e), and the presence of oxygen on the Co particle are more likely due to the physical absorption of atmospheric oxygen from outside exposure. A discussion on the formation of CBNT and MWCNT is presented in the following section.

TEM image of as-synthesized Co/Co_9S_8/CNT in Fig. 3a shows the presence of carbon in two particular forms, CBNT and MWCNT of several micrometer length. The particle morphology and carbon formation in Co/Co_9S_8/CNT in presence of sulfur is quite different than Co/CNT synthesized without sulfur. A close observation shows that bamboo kind carbon tubes consist of hemi-spherical Co/Co_9S_8 particles of 10–20 nm size dispersed over the bamboo walls and boundaries as shown in Fig. 3b. However, the particle in MWCNT are neatly filled with extended metal nanowires where the lattice fringes are parallel to the nanotube axis with an elongated teardrop shape as in Fig. 3c. The majority of Co_9S_8 nanowire encapsulated with MWCNT are 1–5 μm length and 20–40 nm diameter. A detailed examination of MWCNT in Fig. 3c consists of 18–22 graphene walls on both the sides of tube axis along with some discontinuity or wrinkles on the graphene layer (encircled defects), which could be associated with the substitution of external species such as N or S atoms on the graphitic network. These defects possibly increase the overall active sites in the catalysts. The presence of more defective sites in Co/Co_9S_8/CNT is evident from the high I_D/I_G value (Raman spectrum), that moreover facilitate the electron transport capacity and thereby enhances the electrochemical properties. The MWCNT shows an interplanar distance of 0.352 nm, slightly higher than the non-defective CNT with interwall distance of 0.34 nm, which could be due to the existence of highly oriented defective sites on the graphene walls [57]. The HRTEM of the particle shows the crystalline structure, with interplanar distance of 0.578 nm corresponding to the (111) plane of Co_9S_8.

The EDX analysis in Fig. 3(d-g) shows the presence of Co and S uniformly distributed all over the catalyst confirming the Co_9S_8 formation. The EDX line mapping of the particle in Figure S6 (inset) further confirms the presence of Co and S in the entire sample, with Co likely to have a slightly higher concentration than S, pointing to the difference in the atomic ratio of Co:S (9:8) in Co_9S_8. The phase mapping of metal nanowire in Figure S7 shows the uniformity in Co_9S_8 formation. To gain further insight, EDX mapping of another area, where bamboo CNTs are more dominant, is shown in Figure S8. The color distribution of Co and S is not very uniform in the bamboo CNT, with some segregated Co areas, indicating the presence of more Co particle along with some Co_9S_8 nanocomposite.

This section discusses the mechanism CBNT and MWCNT formation in presence of Co metallic nanowire and Co_8S_9 nanoparticles, based on the material characterization and previous reports. Large scale production of CNTs, such as, multiwalled CNT (MWCNT), single walled CNT (SWCNT), bamboo CNT (BCNT), carbon nanofibers (CNF) by following catalytic approach is highly promising owing to a better control in the anisotropic dimension, alignment and helicity of the tube structure [58]. The common routes pursued for the catalytic production of CNTs are: a) chemical vapor deposition (CVD) and decomposition of lower hydrocar-

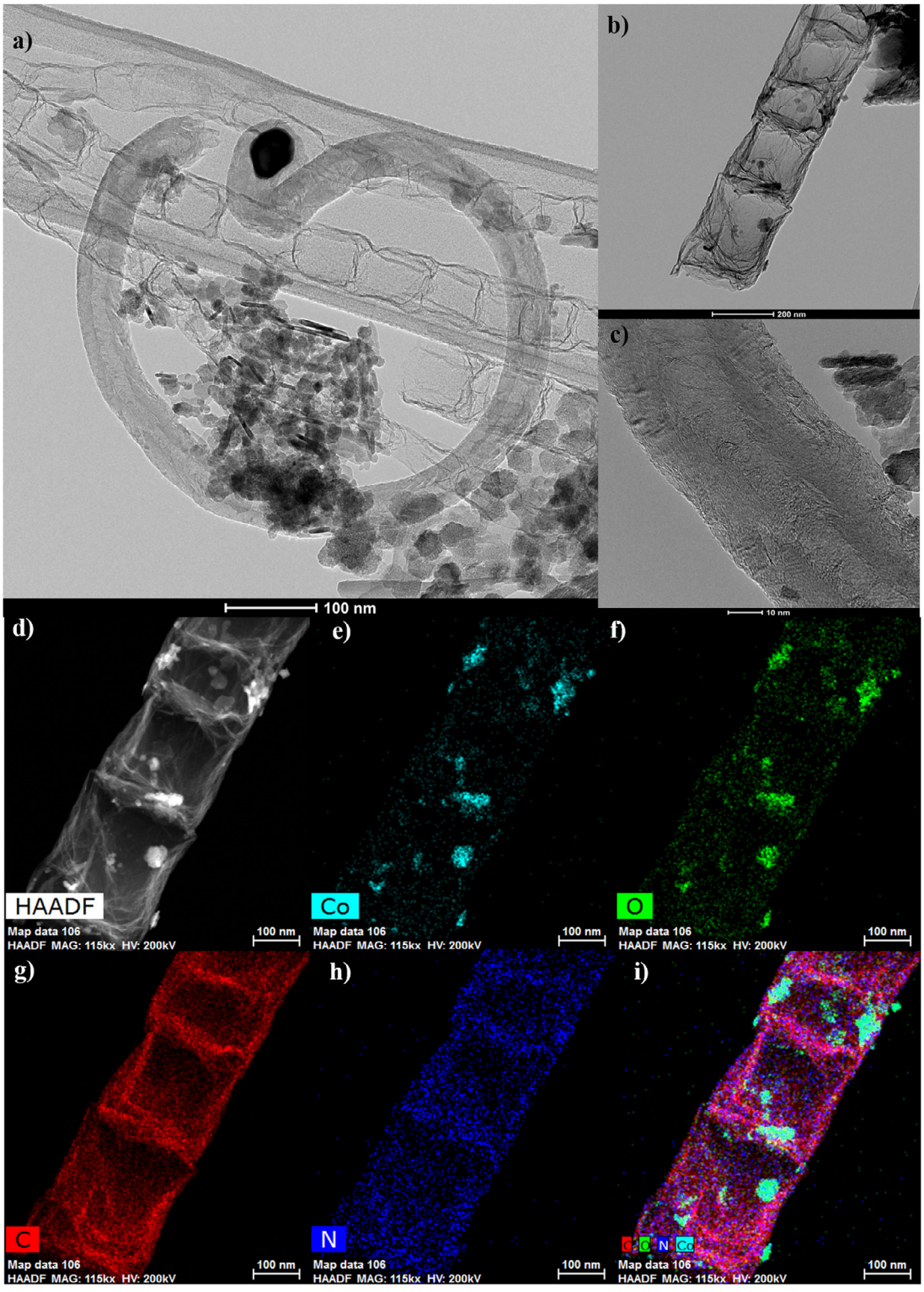

Fig. 2. a) TEM and b) carbon bamboo tube and c) MWCNT presented in Co/CNT and its corresponding HAADF-STEM image and phase mapping as shown in (d-i).

bons in presence of catalytically active substrate [59,60], b) using polymer precursors activated on metallic nanoparticles [61], c) synthesis from the pyrolysis of organometallic reagents along with transition metal salt only as a carbon source or additional hydrocarbon as subagents. In this work, we followed the pyrolysis of melamine in presence of cobalt nitrate and thioamide, where melamine was the main source of C and N, and sulfur atoms were provided by thioamide. Ramaprabhu and team, recently reported the structure, morphology and composition change of melamine at different stages of pyrolysis [62]. The thermal decomposition of melamine starts at 390 °C, through the condensation of melamine into melem adducts that are further converted into melon adduct by the elimination of ammonia group from the ring structure. Eventually, the condensation at 500 °C triggers the conversion of melon into polymeric graphitic carbon nitride (g-C_3N_4) as a first stable form. Layered C_3N_4 resembles graphite which consist of

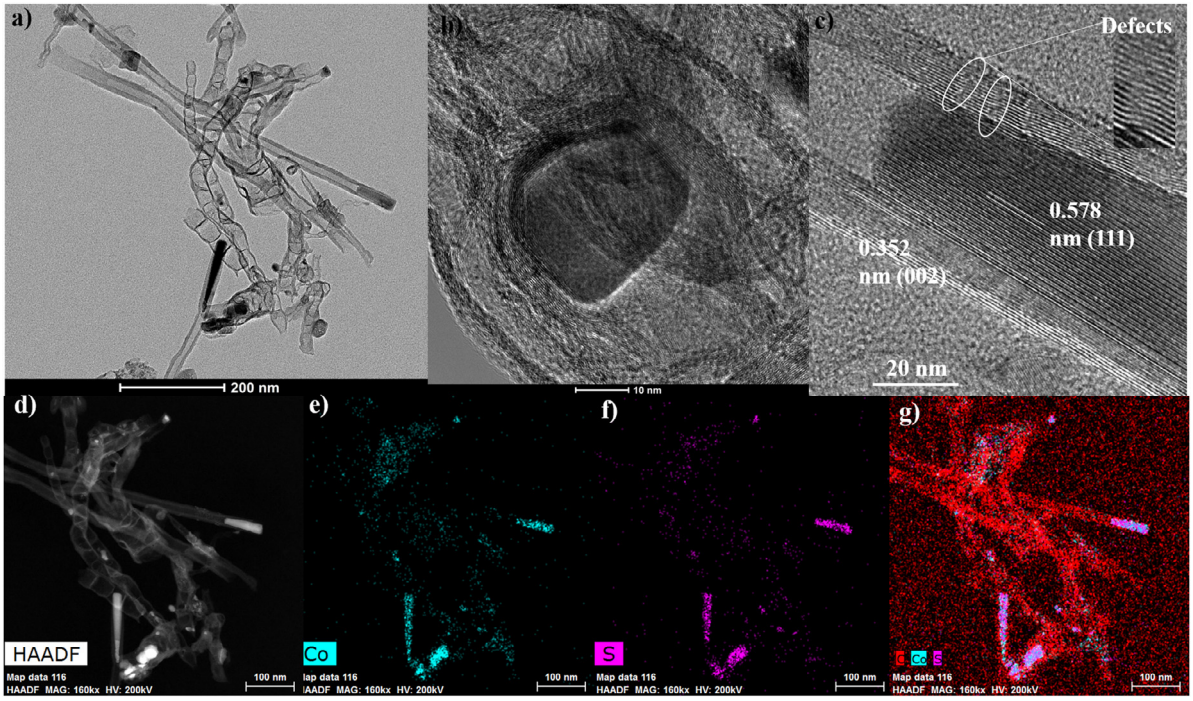

Fig. 3. a) TEM image and closed observation of particles trapped in a) CBNT and b)MWCNT c) TEM image of MWCNT embedded with elongated particle represents the lattice planes and graphene layer carbon defects (enlarged). HAADF-STEM elemental mapping (d-g) of Co/Co_9S_8/CNT.

two main structural unit: tri-s-triazine and s-triazine, along with the π conjugated graphitic planes with C and N atoms linked via sp^2 hybridization [63–65]. Further increase in temperature above 600 °C decomposes the metastable g-C_3N_4 and provide the required C and N atoms as the nucleation source of carbon nanotubes. Concurrently, cobalt nitrate hexahydrate undergoes stepwise thermal decomposition into its different hydrates such as tetra- and di-hydrate, and subsequently complete removal of hydrate to form cobalt oxide followed by amorphous metallic phase and further conversion to metallic cobalt [66]. Thus, the presence of metallic nanoparticle catalyzes the nucleation of carbon nanotubes formation. Dia et al. observed the necessity of Co^{2+} ions for the formation of well-defined carbon nitride nanotube. They found that without the cobalt particle there is no structural transformation of carbon nitride sheets into carbon nitride nanotube [67]. Thereby, the growth mechanism was termed as 'metal-mediated-graphitization'. Leonhardt et al. explained the growth mechanism of metal filled CNT similar to the existing vapor–liquid–solid (VLS) mechanism, where the growth mode (tip growth or root growth) depends on the contact force between the particle and the substrate surface [68].

In-situ growth mechanism is much more complex than ex-situ, as the graphitization of the CNT and the filling of the core with metal nanoparticles occur simultaneously and the nanotube can grow via, either tip mechanism or root mechanism. The growth mechanism of Co_9S_8 nanowires, microstructure and morphology of the catalyst and CNT are greatly influenced by the vapor concentration of thioacetamide. Memon et al. reported a kinetic study of the thermal decomposition of thio-group compound (thiophene) and they found that at higher temperature the pyrolysis of thioamide group was initiated by the fission of C-S bond [69] that followed the production of a mixture containing C_xH_y compound and sulfur containing species (eg: H_2S). Under those conditions, possibly two processes can take place on the surface of the Co catalyst: one is the decomposition and diffusion of C atoms on the surface of the catalyst, and second is the sulfidation of the Co catalyst that resulted in the formation of Co_9S_8. The influence of carbon source on catalyst, may result in the carburization of the catalyst in which the metal surface was converted into metal carbide at the grain boundary of the catalyst as evident from the XPS results in the coming section. However, if the rate of carbon formation on the metal is greater than the energy for the formation of metal carbide, there will be a deactivation in the diffusion of carbon atoms from gas phase into the bulk of the catalyst. Thus, the metal carbide become unstable and decompose. This may be the reason why metal-carbide is not identified in the TEM, somehow the presence of metal-carbide is detected from the XPS analysis [70]. Du et al. explained a new growth mechanism on the filling of the Co_9S_8 nanowire based on the volume increase resulting from the phase transition of Co to Co sulfide [71]. Demoncy et al. conducted a similar study on the filling of CNT with various metal and their direct effect on the presence of Sulfur [72]. The XRD and TEM results show the existence of Co atoms without any phase transformation to Co_9S_8 that could be due to the insufficient thioacetamide vapor concentration for sulfidation reaction. Owing to that, the catalyst contains Co nanoparticles scattered on Bamboo CNT and Co_9S_8 encapsulated in MWCNT. Once the temperature reaches 700 °C, the reactor medium contain C_xH_y and H_2S species from thioacetamide and carbon clusters from the decomposition of melamine. Initially, the carbon atoms from thioacetamide and melamine nucleates and form a carbon shell around the Co catalyst. Meanwhile, H_2S reacts with Co atoms moderately and sulfur atoms nucleate onto the Co surface. The cubic Co catalyst with a unit cell containing four cobalt atoms is transformed into a cubic Co_9S_8 unit cell of 36 Co atom and 32 S atom with an increase of 144% in cell volume than the initial value. Due to this volume expansion during the phase transition (Co to Co_9S_8), a higher pressure is built up between the encapsulated catalyst particle and the carbon shell. The CNT act as a strong nanoscale mold for the excretion and deformation of cobalt sulfide into nanowire. Co_9S_8 nanowire directs the MWCNT to grow straight. In order to obtain long and continuous Co_9S_8 nanowires fully covered with CNT, the growth rate of Co sulfidation

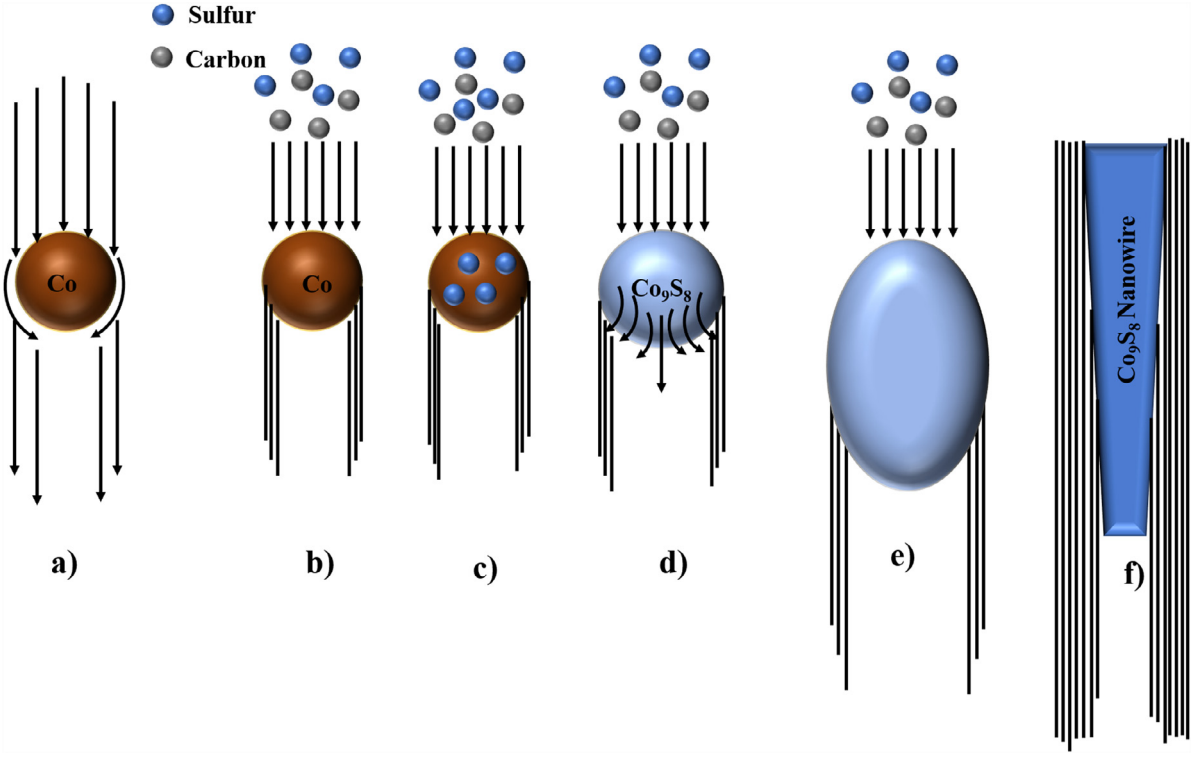

Scheme 1. Schematic representation of the growth mode of MWCNT filled with Co_9S_8 nanowire. a-b) adsorption and diffusion of carbon and sulfide particles c) sulfidation between Co and sulfide species d) volume expansion during the phase transition from Co to Co_9S_8 resulted with increase in internal pressure e) reformation and excretion of catalyst that are encapsulated inside nanoscale CNT mold f) continuous sulfidation and nucleation resulted in Co_9S_8 nanowire.

should be consistent with the nucleation of CNT. If the growth rate of CNT is greater, the tail part of CNT will be unfilled with Co_9S_8 nanowire as shown in Fig. 3c. A detailed mechanism of the pyrolysis of melamine into Co_9S_8 nanowire encapsulated with MWCNT is shown in Scheme 1.

The mechanism of carbon bamboo CNT (CBNT) is slightly different than discussed above. Lin and co-workers conducted a dynamic observation on the development of bamboo like CNT on Ni catalyst during the decomposition of C_2H_2 and postulated a gas-solid mechanism on CNT growth [73]. The carbon atoms diffuse into the cobalt nanoparticle and initiate the formation of inner graphene layer. With time, more carbon atoms are added at the end of the graphene layer and Co nanoparticle become asymmetric and the nucleation of carbon atoms takes place at the upper edge of the disordered Co particle. The shape change of the metal catalyst due to the contact interaction takes place above Tammann Temperature (Co-611 °C) and under pressure, that can be in two ways, one is the sintering under pressure and other is the squeezing of the metal nanoparticle under the graphene conical contact pressure [74]. Various authors reported their own findings on the possible mechanisms on the nanoparticle shape change that facilitates the CBNT formation [75–78]. This initiates the formation of nodes on carbon bamboo nanotube (CBNT). Five to seven graphene layers are added one above another to make the graphene wall thicker and extended around the bottom distorted Co particle. The completed graphene layer makes a hemispherical cap that partition the existing tube internally. During node formation, the elastic elongation of the bottom part of the catalyst increases the effective interface and surface area of the catalyst, that also increases the particle strain energy. Once it reaches the upper limit, particle is ejected from the newly formed bamboo node and the process is repeated to ensure multiple compartments in a single stranded bamboo CNT. The mechanism of CBNT is represented in Scheme 2.

To obtain the surface chemical state and elemental composition of Co/ CNT and Co/Co_9S_8/CNT, X-ray Photoelectron Spectroscopy (XPS) analysis was conducted. In the XPS survey spectrum of Co/Co_9S_8/CNT in Figure S9 shows five sharp peaks at 791, 531, 399, 284 and 162 eV attributed to cobalt (Co), oxygen (O), nitrogen (N), carbon (C) and sulfur (S); whereas the corresponding peak of Sulfur was not seen in Co/CNT survey spectrum. The C and N peaks originate from the CNT substrate and O signal could be from the slight oxidation of Co_9S_8 or the absorbed water (H_2O) from atmosphere [79]. The quantitative analysis of XPS survey spectrum in Table S1 shows a consistency in the elemental composition with the EDX analysis in Figure S2. The decrease in C content in Co/Co_9S_8/CNT, could be due to the sulfur doping that increases the heteroatom defects on the graphene lattice network and decreases the graphitization degree resulting from a decrease in the ordered carbon framework, as evident from Raman spectrum. The high resolution XPS spectra of Co 2p for Co/CNT and Co/Co_9S_8/CNT are shown in Fig. 4a-b. The Co 2p profile consists of two main spin orbital doublets (Co $2p_{3/2}$ and Co $2p_{1/2}$) that are separated with 15.6 eV and two shakeup satellites (denoted as Sat.). In Co/CNT (Fig. 4a), the two main peaks at 780.76 eV and 796.2 eV describe the Co^{2+}state of cobalt, where Co/Co_9S_8/CNT (Fig. 4b) contain similar peaks with a positive shift to higher binding energy at 781.5 eV and 797.2 eV, along with a weak peak corresponding to Co^{3+} at 776.8 eV [79]. The presence of higher oxidation state always facilitates better electron transport and enhances the electrochemical property of the catalyst. In addition, it is worth noting here that there is a positive shift in Co 2p peak of Co/Co_9S_8/CNT when compared to Co/CNT as shown in Figure S10. The peak shift should be due to the strong migration of electron cloud triggered by the high electronegative N or S atoms doped on the CNT substrate that induce strong covalent coupling between the Co species and N doped CNT. Moreover, the incorporation of S atom to the Co lattice enhances the charge transfer between Co and S along with a strong

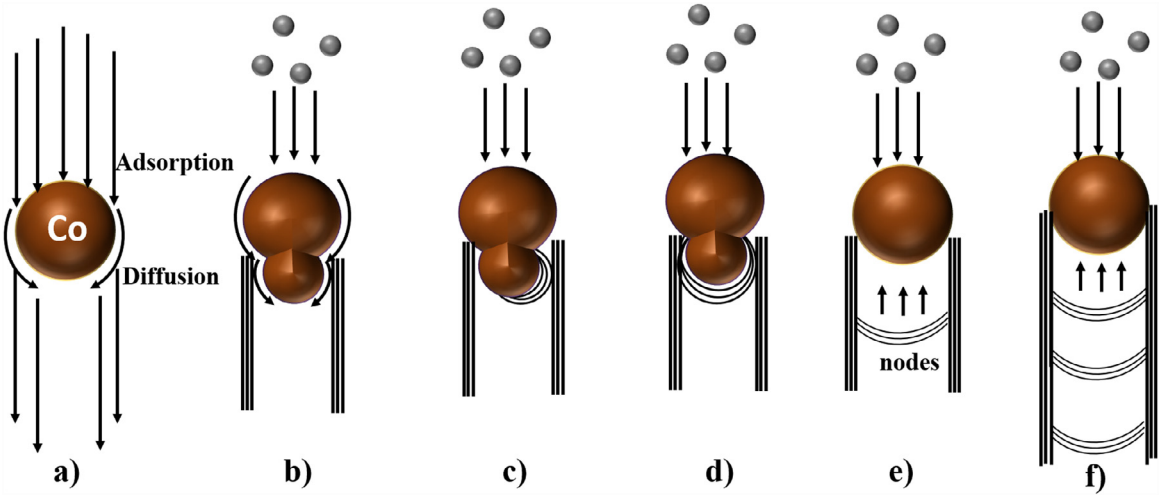

Scheme 2. Schematic diagram showing the stepwise formation of carbon bamboo nanotube (CBNT). a) adsorption and diffusion of carbon b) deformation of particle at bottom side, along with nucleation of graphene layer c) nucleation of bamboo-nodes partially at the interface of deformed particle-graphene wall junction d) nucleated graphene layer extended at the bottom of the particle as more adatoms are added into the deformed particle-graphene wall interface e) formation of hemispherical cap with 5–7 layers of graphene that seal the nanotube internally and the particle contraction forces the particle to release from the newly generated node d) the repeated adsorption nucleation steps resulted with bamboo nanotube of micrometer length.

interaction [45]. These intimate hybridizations of electron transfer species in a nanocomposite renders faster charge transportation favoring the electrochemical reactions. Fig. 4(c-d) shows the core level spectrum of the O 1 s region in Co/CNT and Co/Co_9S_8/CNT. Both profiles consist of three main characteristic peaks centered at 529.8 eV (O_L), 531.2eV(O_v) and 532.9 eV(Oc), correspond to oxygen bonded to metal lattice, non-stoichiometric oxygen generates from oxygen defects and the chemisorbed oxygen from external species respectively [80,81]. In Co/Co_9S_8/CNT, O_v (86.15%) is the most dominating peak with much higher intensity than others (O_L-4.32% and O_C-9.52%). The level of distortion on the crystal surface can be identified from the degree of oxygen defects calculated from the relative area of O_v/O_T, where O_T is the sum of areas of O_L, O_V and O_C. The value of O_v/O_T for Co/CNT and Co/Co_9S_8/CNT are 0.568 and 0.912 respectively, which indicates that the presence of sulfur during synthesis reconstruct the lattice and generates more oxygen vacancies that significantly favor the adsorption/desorption of the reactive species, intermediates and products. Fig. 4 (e-f) displays the high resolution XPS spectrum of carbon (C 1 s) in Co/CNT and Co/Co_9S_8/CNT with five main characteristics peaks at 285.2, 286.1, 287.6, 288.4 and 291.1 eV with a variation in the range of ± 0.3 eV ascribed to the sp^2 hybridized C–C bond on the graphitic honeycomb structured lattice (sp^2 C–C), alkoxy/epoxy form (C–S, C–N, C–O), $C = O$, $O–C = O$ bond formation and pi-pi* (graphitic shakeup satellite) respectively [82]. These results manifest that S and N atoms are successfully doped in the carbon framework. Moreover, a minor peak present in Co/Co_9S_8/CNT at 283.6 eV corresponds to the metal carbide peak, which could be from the interface of nanoparticle/graphene layer as explained in the proposed mechanism. The chemical state of doped N atom can be identified using the high-resolution N 1 s spectrum of Co/CNT and Co/Co_9S_8/CNT as in Figure S11. The three main characteristic peaks centered at 389.9 eV (399.1 eV), 401.2 eV (401.4 eV) and 403.5 eV(403.8 eV) are respectively attributed to the Pyridinic N, Graphitic N and higher oxidation state of N, respectively for Co/CNT (Co/Co_9S_8/CNT). Pyridinic N bonding originates from the sp^2 hybridized π bonding of N atoms to the two neighboring C atoms (sp^2 hybridized) that contributes one p-electron at the edges (or defects) of graphene network. Graphitic N configuration suggests the bonding of sp^2 hybridized N atoms with three sp^2 hybridized neighboring C atoms. Pyridinic N bond could donate one p electron to the aromatic π bond of the carbon atom, thereby improving the electron conductivity of graphene lattice. Moreover graphitic N promotes a charge delocalization, that improves the chemisorption property of the active sites of the catalyst. It was previously reported that Pyridinic N and Graphitic N play a great role in the catalytic activity, so the doping of N atom to the carbon framework is critical for electrochemical property enhancement. Furthermore, the peak position shows a slight positive shift in each peak of N bonding of Co/Co_9S_8/CNT suggesting a strong interaction through covalent coupling between N–C-transition metal, compared to Co/CNT [83,84].

The high-resolution spectrum of S 2p for Co/Co_9S_8/CNT in Figure S12 was fitted into five curves that indicate three different forms of sulfur species. The deconvoluted peaks at 162.1 eV and 163.5 eV can be attributed to S $2p_{3/2}$ and S $2p_{1/2}$ region respectively that originate from the cobalt sulfide. The peak at 165.1 eV can be assigned to the C-S-C and the peaks at 168.6 and 169.9 eV can be related to the high oxidation state of sulfur (due to the incomplete reduction of the sulfate). These results affirm the existence of sulfur atoms doped over the carbon lattices, which generate a spin density through a mismatch of the outer orbitals of carbon and sulfur that act as a synergetic factor for the faster charge transfer in electrochemical reaction.

While taken together, these XPS results demonstrate the successful formation of heteroatom doped carbon framework (CNTs) covalently coupled with Co_9S_8 nanoparticles that could improve the electron conductivity and physiochemical properties to favor the overall electrochemical properties significantly.

4. Electrochemical characterization

HER activities of Co/CNT and Co/Co_9S_8/CNT electrode in 1 M KOH electrolyte was performed by linear sweep voltammetry (LSV) at a scan rate of 5 mVs^{-1} and compared with the commercial Pt/C (20%) electrode as shown in Fig. 5a. In Co/Co_9S_8/CNT, it is noteworthy that the steady state current starts to rise beyond –0.1 V and causes a dramatic increase in the current density when sweeping at higher negative potential. As shown in Fig. 5a, Co/Co_9S_8/CNT can produce a current density of 10 $mAcm^{-2}$ at lower overpotential of 200 mV, while for Co/CNT it required 298 mV to attain the same current density. The Tafel slope is another kinetic parameter to evaluate the electrocatalytic mechanism for HER/OER. The linear Tafel plot was measured using the Tafel equation ($\eta = a + b^*\log(j)$),

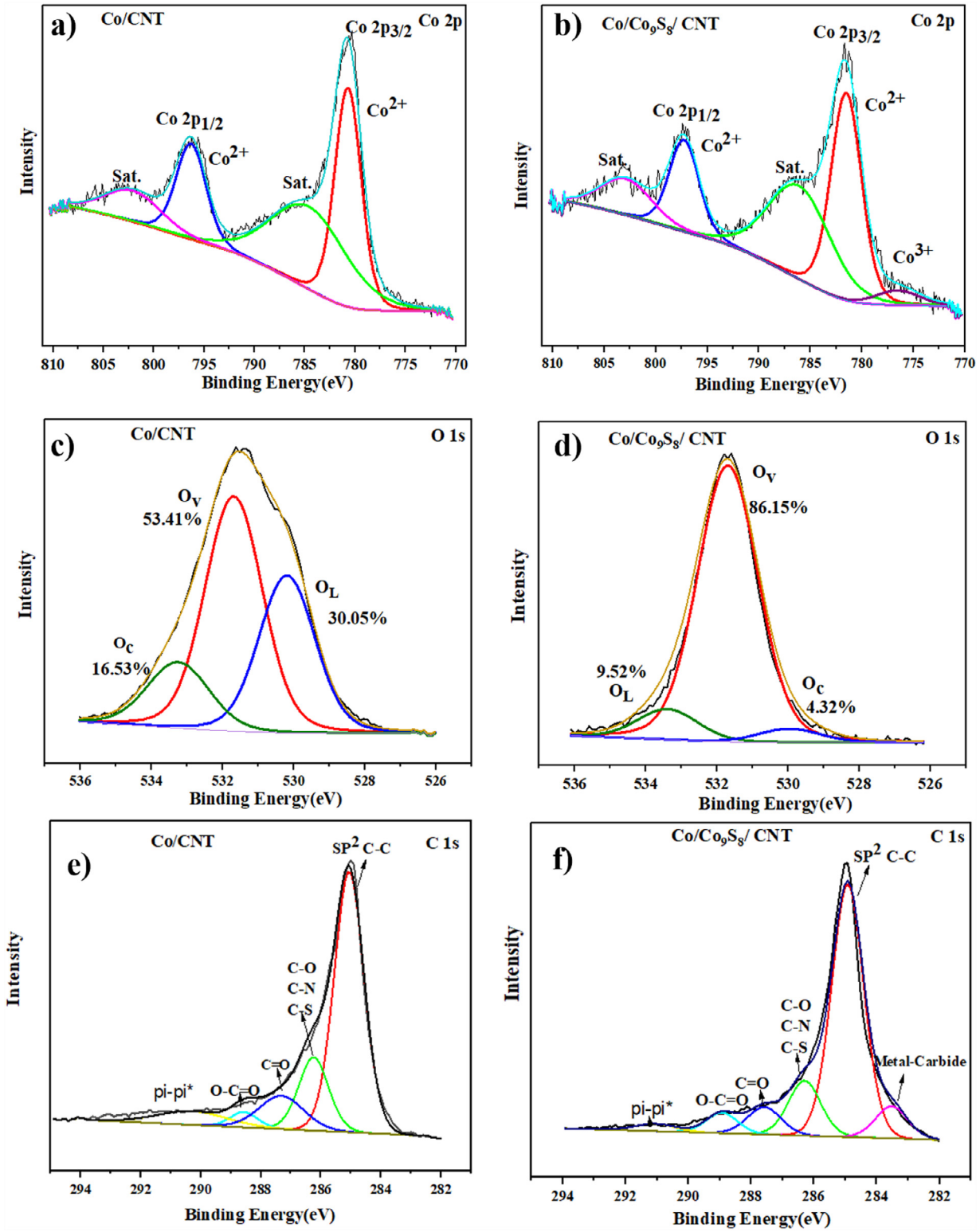

Fig. 4. (a-b) Co 2p (c-d) O 1 s and (e-f) C 1 s high resolution XPS spectrum of as-synthesized Co/CNT and Co/Co_9S_8/CNT.

where j is the current density, a is the exchange current density, b be the Tafel slope and η be the measured over potential. A lower Tafel slope indicates a higher hydrogen evolution at lower overpotentials. Tafel slope of Co/Co_9S_8/CNT (90 $mVdec^{-1}$) is much lower than Co/CNT(152 $mVdec^{-1}$) signifying a more favorable kinetics and faster electron transfer during HER reaction after the sulfur doping. Stability is another most significant parameter to evaluate the quality of the catalyst that can be performed using chronoamperometric (CA) experiments. The CA profile in Fig. 5c shows that Co/Co_9S_8/CNT maintain a constant current of 10 $mAcm^{-2}$ at 200 mV even after 20 h, which indicates a good durability of the catalyst under alkaline medium. The fluctuation of current (Fig. 5c, inset) in a tolerable level is due to the evolution of H_2 gas that hinder the passage of electron to some

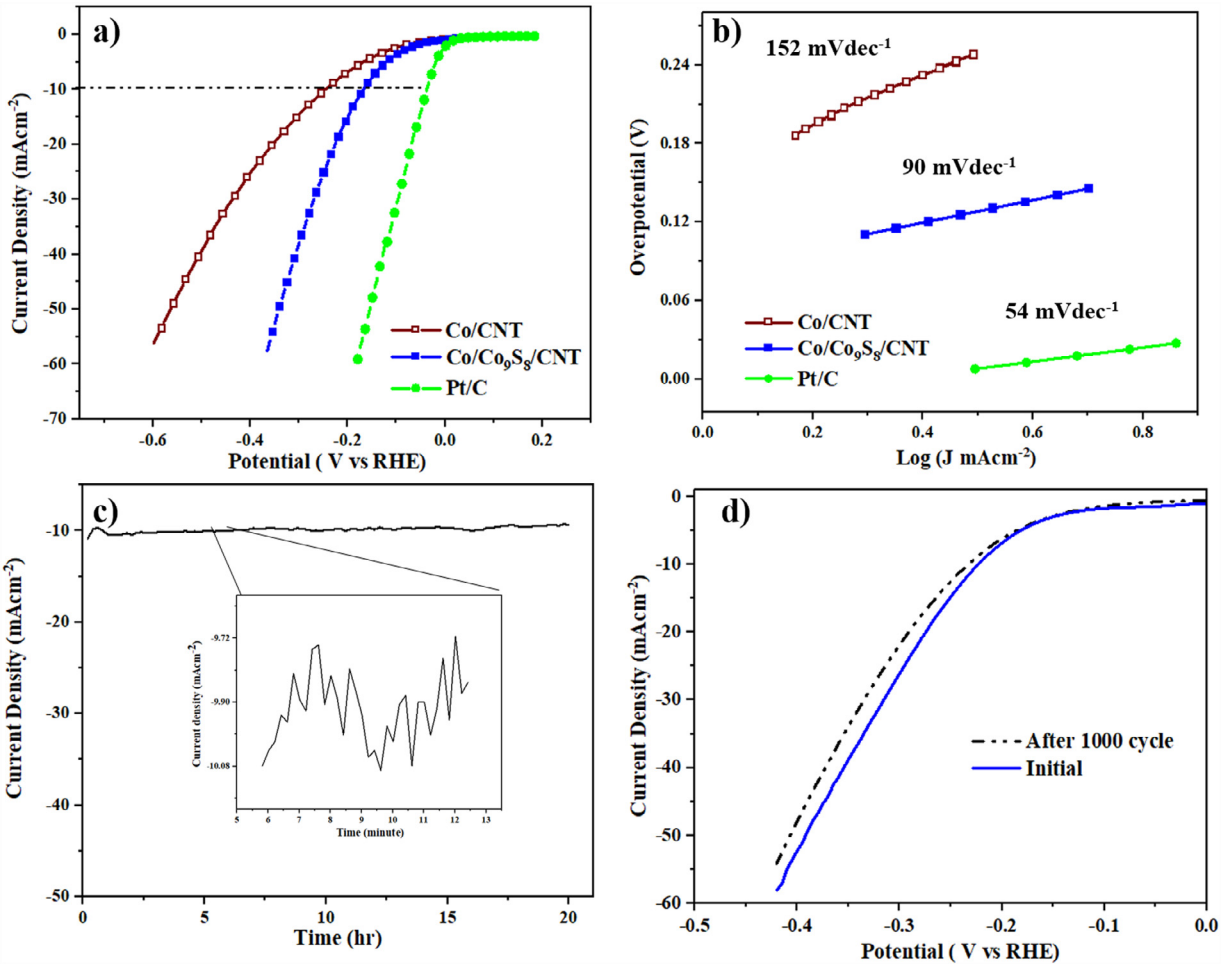

Fig. 5. a) LSV polarization curve b) Tafel plot of Co/CNT and Co/Co_9S_8/CNT and commercial Pt/C (20%) corresponds to HER at a scan rate of 5 mVs^{-1} and c) Chronoamperometric profile of Co/Co_9S_8/CNT at −0.2 V for 20 hr d) polarization curve recorded for Co/Co_9S_8/CNT before and after 1000 cycle of CV stability run in 1 M KOH solution.

extent. The durability and stability of Co/Co_9S_8/CNT can be further confirmed by 1000 continuous accelerated CV cycle runs and performing the polarization curves before and after the sweep experiments, as displayed in Fig. 5d. The polarization after 1000 cycle shows only a slight shift in current profile of about 5 mV towards the negative direction, but follows a constant current value during the entire potential sweep, which confirms the excellent stability and durability of Co/Co_9S_8/CNT in HER application. Electrochemical impedance spectroscopy (EIS) is carried out to gain more insight on the HER kinetics. The Nyquist plot (Figure S13) shows a greater arc radius in Co/CNT than Co/Co_9S_8/CNT and confirms that the charge transfer resistance of Co/Co_9S_8/CNT is significantly lower compared to Co/CNT, suggesting a faster charge transfer mechanism owing to greater surface area, larger pore size and unique electronic structure. These finding suggest that Co/Co_9S_8/CNT can serve as a new category of HER electrocatalyst with exceptional activity and excellent durability.

Further investigation was conducted to assess the OER performance of Co/CNT and Co/Co_9S_8/CNT in 1 M KOH solution. The LSV profile of OER in Fig. 6a shows an oxidation peak around 1.3–1.4 V that can be attributed to the oxidation of Co^{3+} to its higher oxidation state of Co^{4+} as previously reported. However, such an oxidation peak was not seen in Co/CNT electrocatalyst. The anodic current of 10 $mAcm^{-2}$ recorded on Co/Co_9S_8/CNT presents a lower onset potential of 1.5 V whereas Co/CNT affords a slightly more positive value at (1.64 V). As shown in Fig. 6b, the Tafel slope of Co/Co_9S_8/CNT and Co/CNT were 79 $mVdec^{-1}$ and 103 $mVdec^{-1}$ respectively. The lower Tafel slope of Co/Co_9S_8/CNT implies its higher OER performance. Stability measurement was conducted on Co/Co_9S_8/CNT to understand the long-term behavior of the catalysts by performing CA and polarization analysis to assess the stability and durability. Fig. 6c shows a stable current density with negligible fluctuations upto 20 h at a constant applied potential 1.5 V, and indicates the kinetic performance on Co/Co_9S_8/CNT catalyst to be highly stable. Furthermore, the LSV curve obtained after 1000 cycles of CV sweeps in Fig. 6d shows no significant change in the anodic current density before and after CV runs and affirms the robustness of Co/Co_9S_8/CNT as a suitable electrode material in electrocatalytic oxygen evolution. However, after 1000 cycles, the oxidation peak around 1.3–1.4 V disappeared due to the complete conversion of Co^{3+} to Co^{4+}, that improves the electrophilicity of the catalyst surface and promotes the adsorption of nucleophilic species such as OH^- for the conversion to OOH^- intermediates [80]. Using EIS we evaluated the enhancement in the electron transportation in Co/Co_9S_8/CNT, where the semicircular diameter of Nyquist plot is much smaller than Co/CNT, owing to lower contact and charge transfer resistance as shown in Fig. 6d. EIS Nyquist plot for Co/Co_9S_8/CNT at different potential plotted as in Figure S14, depicts a wider semicircular diameter with decrease in applied potential from 1.6 to 1.4 V. A simple Randle circuit model developed in Inset (Figure S14) used to fit the Nyquist Plot consist of series resistance (R_s) corresponding to the overall electrolyte resistance, constant phase element (CPE) used instead of double layer capacitance (C_{dl}) and charge transfer resistance (R_{ct})

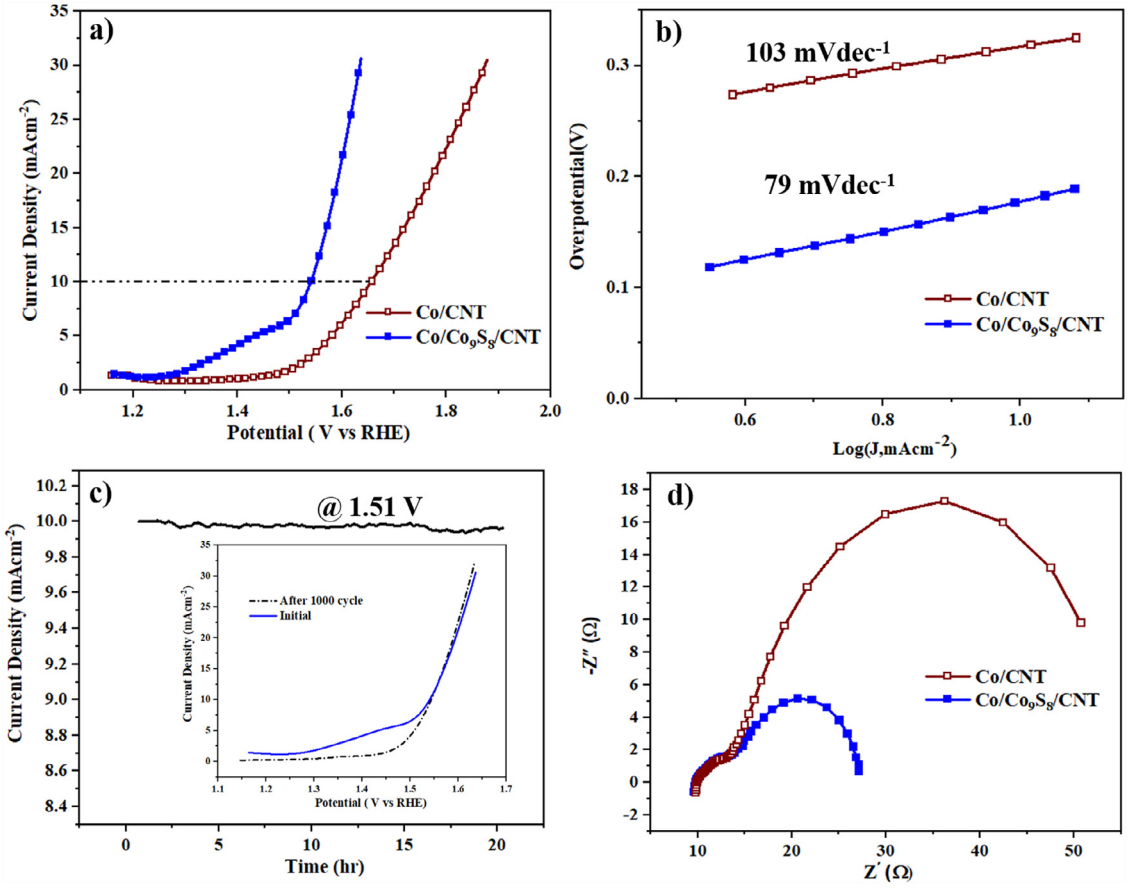

Fig. 6. a) OER Oxygen evolution reaction (OER) LSVs at a sweep rate of 5 mVs $^{-1}$ and (b) Tafel plots of Co/CNT and Co/Co_9S_8/CNT and commercial Pt/C (20%) at a scan rate of 5 mVs^{-1} c) The electrochemical durability with current-time profile of Co/Co_9S_8/CNT at 1.51 V . Inset shows the LSV cureve before and after 1000 CV cycle d) The electrochemical impedance spectra recorded at 1.6 V of Co/CNT and Co/Co_9S_8/CNT in 1 M KOH solution.

owing to the resistance at catalyst-electrolyte interface, which can be measured from the diameter of the fitted semicircle, more likely to be inversely proportional to the rate of overall charge transfer during OER mechanism. The R_s value of Co/Co_9S_8/CNT (5.8 Ω) was much smaller than Co/CNT(11.6 Ω), also R_{ct} of Co/Co_9S_8/CNT (21 Ω) and Co/ CNT (32 Ω) follows a similar trend resulting with a faster electron transfer and charge kinetics for oxygen evolution reaction on Co/Co_9S_8/CNT. These results confirmed Co/Co_9S_8/CNT to be a promising catalyst with superior activity and stability towards OER in alkaline medium. Our findings suggest that excellent performance of Co/Co_9S_8/CNT could have benefited from strongly integrated Co_9S_8 metallic nanowire on the N doped MWCNT with high electronic conductivity.

Figure S16.a shows the ring and disk current along with applied disk potential and constant ring potential (0.4 V RHE) of RRDE measurement to estimate the faradaic efficiency of the Co/Co_9S_8/CNT in 1 M KOH solution. It is observed that the faradaic efficiency is maximum 99.4% at the applied disk potential of 1.50 V and decreases to 66.7% with the increase in potential to 1.60 V. The decrease in the faradaic efficiency towards higher potential is due a decrease in the ratio of ring to disk electrode currents, where the ring electrode effectively collects the large oxygen bubbles formed over the surface of the disk. A similar trend of decrease in the faradaic efficiency at higher potential is reported elsewhere [53–55]. The electrode at higher potential shows presence of large bubbles on the disk electrode without completely dissolving the formed oxygen in the electrolyte. In that context, faradaic efficiency of 99% at 1.5 V is considered as the electrocatalyst OER efficiency, by ignoring the decrease in the efficiency at higher potential. The current profile in Figure S16.b closely monitors the H_2O_2 generation at the ring potential held at 1.4 V. There is no detectable current in the ring, which shows that the oxidation of H_2O_2 does not take place on the ring and no H_2O_2 species were formed. These results confirm that OER at Co/Co_9S_8/CNT in 1 M KOH solution proceeds to generate di-oxygen via 4 electron transfer mechanism ($4OH^- \rightarrow O_2 + 2H_2O + 4e^-$).

a) Based on the excellent OER and HER results discussed above, dual functionality of our electrode is anticipated. Controlling the spontaneous directional motion of water molecule in nanoscale is critical for the water splitting to generate hydrogen and oxygen. Chen et al. proposed the stiffness gradient on the surface of CNTs that governs the spontaneous directional motion of the water molecule [85]. Water permutation rate is greatly affected by the structure of CNTs and dopant atoms. In 2012, Li et al. studied the water permeation effect over the nitrogen doped CNTs and they found that water-nanotube interaction can be greatly tuned by doping nitrogen atom into the nanotube walls [86]. Although in MWCNTs, number of layers and nanotube type greatly controlled the water transportation behavior towards the active metal species embedded inside the CNTs [87,88].

We constructed a two-electrode electrolyzer to evaluate the overall water splitting performance of Co/CNT and Co/Co_9S_8/CNT, by using them as electrodes (both anode and cathode containing the same catalyst) as illustrated in Fig. 7a. Interestingly, as shown in Fig. 7b, Co/Co_9S_8/CNT and Co/CNT can deliver a current density of 10 $mAcm^{-2}$ at room temperature at an applied cell volt-

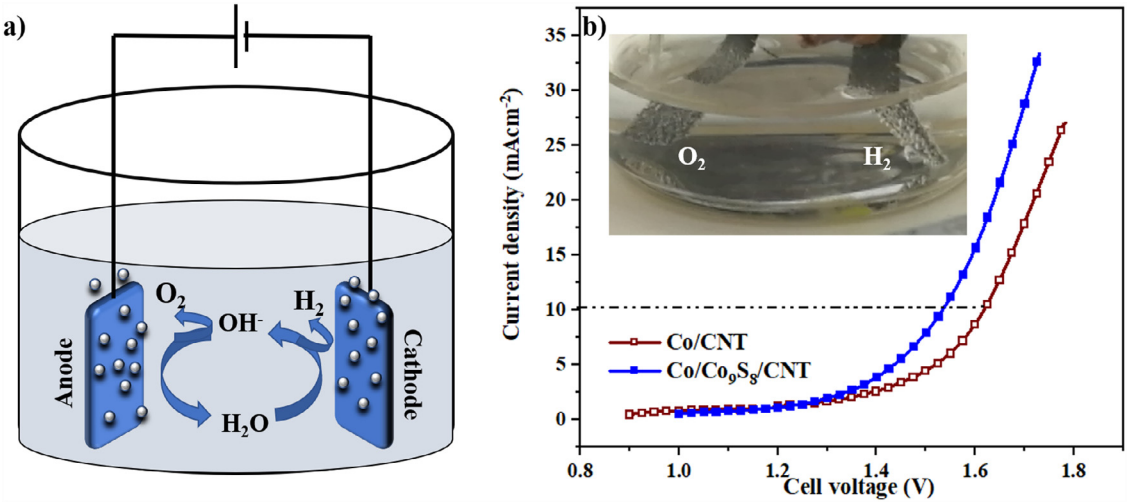

Fig. 7. a) Schematics diagram showing the construction of an overall-water-splitting electrolyzer with anode and cathode as same catalysts b) LSV polarization curve of overall water splitting at room temperature. Inset shows the real time image with cathode and anode electrode with the evolution of H_2 and O_2 bubbles on the Co/Co_9S_8/CNT loaded carbon cloth.

age of 1.5 V and 1.62 V, respectively, which shows a great improvement compared to the benchmark of IrO_2 (1.58 V) and Pt (1.77 V) catalysts. The optical image in Fig. 7b shows the formation of H_2 and O_2 bubbles on the surface of catalyst loaded carbon cloth, indicating a superior performance of Co/Co_9S_8/CNT towards overall water splitting in alkaline medium. As shown in Figure S16, Co/Co_9S_8/CNT can deliver a constant current density of 10 mAcm^{-2}, without any decay at a constant voltage of 1.5 V over 22 h of electrolysis experiment. TEM analysis of Co/Co_9S_8/CNT in Figure S17 after the long-term stability shows that the morphology and structure remain unchanged, and the same structure with long and continuous Co_9S_8 nanowire fully covered with CNT is visible. These results show a superior activity, stability and durability of Co/Co_9S_8/CNT catalyst that promises a great potential for large scale applications.

Figure S18 shows the effect of concentration on the overall water splitting reaction over Co/Co_9S_8/CNT loaded carbon cloth. The applied cell voltage to deliver the current density of 10 mAcm^{-2} at room temperature shows an inverted volcanic trend that holds 1.65 V, 1.5 V and 1.6 V for 0.1 M, 1 M and 4 M KOH respectively. With an increase in the solute concentration, the diffusion coefficient gets smaller due to an increase in viscosity. However, the activity of the catalyst in a neutral solution is comparatively low, which shows that water splitting is limited in normal water and requires an ionic medium for the charge transportation. Electrolyte engineering for OER and HER apparently improve the overall water splitting by enhancing the mass-transport flux that influences the intrinsic catalytic property. Shinagawa et al. conducted a detailed investigation on the electrolyte engineering that shows a clear boundary on the reactant selectivity towards H_2O/OH^- reaction due to diffusion limitation of OH^- and its contribution towards the mass transport of the buffered species in mild pH conditions [89]. Tavakkoli and coworkers measured the OER polarization curve of γ-Fe_2O_3/CNTs in 1 M and 0.1 M NaOH and reported the potential required to obtain a current density of 10 mAcm^{-2} to be 1.57 V and 1.61 V respectively [90].

Based on the previous analysis, the outstanding performance of Co/Co_9S_8/CNT towards overall water splitting can be attributed to the following factors.

a) The hierarchical Co/Co_9S_8/CNT nanostructure with larger surface area and high porosity ensures the exposure of active sites for catalytic reaction and prevents the stacking of graphene layers that greatly facilitate a faster diffusion of electrolyte, adsorption/desorption of product and intermediates which accelerates the subsequent surface electrochemical reaction [91].
b) Presence of carbon nanotubes, either CBNT or MWCNT, provide excellent electron conductivity to the electrode that helps in the enhancement of charge transportation.
c) Higher percentage of graphitic and pyridinic N improves the electrochemical property of Co/Co_9S_8/CNT. Decorating graphene with graphitic and pyridinic N atom reduces the work function, enhances the electronic property, increases the pore affinity for the aqueous electrolyte, and improves the electronic conductivity. All these factors, combined together, result in a further enhancement in the electrochemical catalytic properties [92,93].
d) The presence of Co in its higher oxidation state in Co/Co_9S_8/CNT always facilitate a faster electron transfer during a catalytic reaction.
e) The excess of anion vacancies (oxygen vacancies, anion dopant and interstitials) in Co/Co_9S_8/CNT compared to Co/CNT can significantly modify the electronic structure and improve the stability of adsorbed intermediate molecule that greatly enhances the electrocatalytic property of the catalyst surface. Moreover, it promotes the surface affiliation to OH^- ion and lowers the energy required for the formation of O^- on the surface [94,95].
f) The hierarchical Co_8S_9 metallic nanowire architecture trapped between the multiple sheets of graphene layers in N doped MWCNT develop a metal-carbon synergistic interaction accounting for its excellent catalytic performance.

Based on the aforementioned results, Co/Co_9S_8/CNT displays enhanced catalytic performance towards the overall water splitting reaction with a long term stability, endowing it as a promising future electrocatalyst for practical application. To our knowledge, the catalytic performance of Co/Co_9S_8/CNT is comparable and even superior to the state-of-the-art non-precious transition metal electrocatalyst (as compared in Table S2).

Conclusion

In this work, we have reported a comprehensive study on the fabrication of Co_9S_8 nanowire on MWCNTs (Co/Co_9S_8/CNT) that can be used as a bifunctional electrocatalyst for OER and HER and finally as an overall water electrolyzer. We followed simple, scalable and economical pyrolysis method in presence of melamine and Co-salt for the preparation of Co/CNT and adding sulfur source

in the mixture resulted in Co/Co_9S_8/CNT. The higher surface area and hierarchical porosity of Co/Co_9S_8/CNT (78.23 $m^2\ g^{-1}$) provides abundant active sites and facilitates mass transfer of reactants and products. The doped heteroatoms on graphene network, specifically Graphitic N, Pyridinic N and thioamide S atoms along with Co_9S_8 metallic nanowire provide abundant active sites for overall water electrolysis. Co/Co_9S_8/CNT serves both, as anode and cathode of two-cell water electrolyzer requiring a cell voltage of only 1.5 V to achieve a current density 10 $mAcm^{-2}$, showed excellent durability in prolonged 22 h water electrolysis in alkaline medium. Owing to the readily scalable synthesis technique, unique electronic and structural properties, superior electrocatalytic performance with excellent stability; Co/Co_9S_8/CNT promises to be a highly desirable electrocatalyst for both anode and cathode for overall water splitting in basic medium.

Declaration of Competing Interest

The authors declare that they have no known competing financial interests or personal relationships that could have appeared to influence the work reported in this paper.

Acknowledgment

This publication was made possible by NPRP Grant (NPRP8–145–2–066) from the Qatar National Research Fund (a member of Qatar Foundation). The statements made herein are solely the responsibility of the author(s). The authors also wish to gratefully acknowledge Centre of Advanced Materials (CAM) and Gas Processing Center (GPC) at Qatar University for XRD and XPS analysis respectively. The SEM analysis was accomplished in the Central Laboratories Unit, Qatar University. The authors would also like to acknowledge QEERI Core Labs for their support related to the TEM characterization. Open Access funding provided by the Qatar National Library.

Data availability

The raw data required to reproduce these findings cannot be shared at this time as the data also forms part of an ongoing study. The processed data required to reproduce these findings cannot be shared at this time as the data also forms part of an ongoing study.

Credit Author Statement

Anchu Ashok: Conceptualization, Methodology, Data curation, Formal analysis, Investigation, Validation, Writing – Original draft

Anand Kumar: Conceptualization, Supervision, Writing – Review & Editing, Project administration, Funding acquisition

Janarthanan Ponraj: Visualization, Investigation

Said A. Mansour: Visualization, Investigation

Supplementary materials

Supplementary material associated with this article can be found, in the online version, at doi:10.1016/j.electacta.2020.137642.

References

[1] E. Antolini, E.R. Gonzalez, Alkaline direct alcohol fuel cells, J. Power Sources. 195 (2010) 3431–3450, doi:10.1016/j.jpowsour.2009.11.145.
[2] R. Bashyam, P. Zelenay, A class of non-precious metal composite catalysts for fuel cells, Nature 443 (2006) 63–66, doi:10.1038/nature05118.
[3] M.L. Perry, T.F. Fuller, A historical perspective of fuel cell technology in the 20th century, J. Electrochem. Soc. 149 (2002) S59, doi:10.1149/1.1488651.
[4] Y. Li, M. Gong, Y. Liang, J. Feng, J.E. Kim, H. Wang, G. Hong, B. Zhang, H. Dai, Advanced zinc-air batteries based on high-performance hybrid electrocatalysts, Nat. Commun. (2013) 4, doi:10.1038/ncomms2812.
[5] A. Ashok, A. Kumar, R.R. Bhosale, F. Almomani, M.A.H. Saleh Saad, S. Suslov, F. Tarlochan, Influence of fuel ratio on the performance of combustion synthesized bifunctional cobalt oxide catalysts for fuel cell application, Int. J. Hydrog. Energy. (2019) 436–445, doi:10.1016/j.ijhydene.2018.02.111.
[6] A. Ashok, A. Kumar, R.R. Bhosale, F. Almomani, S.S. Malik, S. Suslov, F. Tarlochan, Combustion synthesis of bifunctional $LaMO_3$ (M = Cr, Mn, Fe, Co, Ni) perovskites for oxygen reduction and oxygen evolution reaction in alkaline media, J. Electroanal. Chem. 809 (2018) 22–30, doi:10.1016/j.jelechem.2017.12.043.
[7] A. Ashok, A. Kumar, J. Ponraj, S.A. Mansour, Preparation of mesoporous/microporous $MnCo_2O_4$ and Nanocubic $MnCr_2O_4$ using a single step solution combustion synthesis for bifunction oxygen electrocatalysis, J. Electrochem. Soc. 167 (2020) 054507, doi:10.1149/1945-7111/ab679d.
[8] A. Ashok, A. Kumar, M.A. Matin, F. Tarlochan, Synthesis of highly efficient bifunctional Ag/Co_3O_4 catalyst for oxygen reduction and oxygen evolution reactions in alkaline medium, ACS Omega 3 (2018) 7745–7756, doi:10.1021/acsomega.8b00799.
[9] M. Zhu, Z. Zhang, H. Zhang, H. Zhang, X. Zhang, L. Zhang, S. Wang, Hydrophilic cobalt sulfide nanosheets as a bifunctional catalyst for oxygen and hydrogen evolution in electrolysis of alkaline aqueous solution, J. Colloid Interface Sci. 509 (2018) 522–528, doi:10.1016/j.jcis.2017.09.076.
[10] J. Masa, P. Weide, D. Peeters, I. Sinev, W. Xia, Z. Sun, C. Somsen, M. Muhler, W. Schuhmann, Amorphous cobalt boride (Co_2B) as a highly efficient nonprecious catalyst for electrochemical water splitting: oxygen and hydrogen evolution, Adv. Energy Mater. 6 (2016), doi:10.1002/aenm.201502313.
[11] A. Ashok, A. Kumar, J. Ponraj, S.A. Mansour, F. Tarlochan, Highly active and stable bi-functional $NiCoO_2$ catalyst for oxygen reduction and oxygen evolution reactions in alkaline medium, Int. J. Hydrog. Energy. 44 (2019) 16603–16614, doi:10.1016/j.ijhydene.2019.04.165.
[12] J. Li, M. Yan, X. Zhou, Z.Q. Huang, Z. Xia, C.R. Chang, Y. Ma, Y. Qu, Mechanistic insights on ternary Ni2−xCoxP for hydrogen evolution and their hybrids with graphene as highly efficient and robust catalysts for overall water splitting, Adv. Funct. Mater. 26 (2016) 6785–6796, doi:10.1002/adfm.201601420.
[13] A. Ashok, A. Kumar, M.A. Matin, F. Tarlochan, Probing the effect of combustion controlled surface alloying in silver and copper towards ORR and OER in alkaline medium, J. Electroanal. Chem. 844 (2019) 66–77, doi:10.1016/j.jelechem.2019.05.016.
[14] S. Xu, H. Zhao, T. Li, J. Liang, S. Lu, G. Chen, S. Gao, A.M. Asiri, Q. Wu, X. Sun, Iron-based phosphides as electrocatalysts for the hydrogen evolution reaction: recent advances and future prospects, J. Mater. Chem. A. 8 (2020) 19729–19745, doi:10.1039/d0ta05628f.
[15] L. Zhao, X.L. Sui, J.L. Li, J.J. Zhang, L.M. Zhang, Z.B. Wang, 3D hierarchical pt-nitrogen-doped-graphene-carbonized commercially available sponge as a superior electrocatalyst for low-temperature fuel cells, ACS Appl. Mater. Interfaces. 8 (2016) 16026–16034, doi:10.1021/acsami.6b03520.
[16] H.W. Liang, X. Cao, F. Zhou, C.H. Cui, W.J. Zhang, S.H. Yu, A free-standing Pt-nanowire membrane as a highly stable electrocatalyst for the oxygen reduction reaction, Adv. Mater. 23 (2011) 1467–1471, doi:10.1002/adma.201004377.
[17] E. Antolini, Iridium as catalyst and cocatalyst for oxygen evolution/reduction in acidic polymer electrolyte membrane electrolyzers and fuel cells, ACS Catal 4 (2014) 1426–1440, doi:10.1021/cs4011875.
[18] J. Greeley, I.E.L. Stephens, A.S. Bondarenko, T.P. Johansson, H.A. Hansen, T.F. Jaramillo, J. Rossmeisl, I. Chorkendorff, J.K. Nørskov, Alloys of platinum and early transition metals as oxygen reduction electrocatalysts, Nat. Chem. 1 (2009) 552–556, doi:10.1038/nchem.367.
[19] J. Zhang, M.B. Vukmirovic, Y. Xu, M. Mavrikakis, R.R. Adzic, Controlling the catalytic activity of platinum-monolayer electrocatalysts for oxygen reduction with different substrates, Angew. Chem. - Int. Ed. 44 (2005) 2132–2135, doi:10.1002/anie.200462335.
[20] S. Kumar, S. Chinnathambi, N. Munichandraiah, Ir nanoparticles-anchored reduced graphene oxide as a catalyst for oxygen electrode in Li-O2 cells, New J. Chem. 39 (2015) 7066–7075, doi:10.1039/c5nj01124h.
[21] Y. Kim, J.H. Park, J.G. Kim, Y. Noh, Y. Kim, H. Han, W.B. Kim, Ruthenium oxide incorporated one-dimensional cobalt oxide composite nanowires as lithium–oxygen battery cathode catalysts, ChemCatChem 9 (2017) 3554–3562, doi:10.1002/cctc.201700560.
[22] X. Li, R. Zhang, Y. Luo, Q. Liu, S. Lu, G. Chen, S. Gao, S. Chen, X. Sun, A cobalt-phosphorus nanoparticle decorated N-doped carbon nanosheet array for efficient and durable hydrogen evolution at alkaline pH, Sustain. Energy Fuels. 4 (2020) 3884–3887, doi:10.1039/d0se00240b.
[23] A. Ashok, A. Kumar, J. Ponraj, S.A. Mansour, F. Tarlochan, Enhancing the electrocatalytic properties of LaMnO3 by tuning surface oxygen deficiency through salt assisted combustion synthesis, Catal. Today. (2020), doi:10.1016/j.cattod.2020.05.065.
[24] Z. Wu, D. Nie, M. Song, T. Jiao, G. Fu, X. Liu, Facile synthesis of Co-Fe-B-P nanochains as an efficient bifunctional electrocatalyst for overall water-splitting, Nanoscale 11 (2019) 7506–7512, doi:10.1039/c9nr01794a.
[25] M. Song, Z. Zhang, Q. Li, W. Jin, Z. Wu, G. Fu, X. Liu, Ni-foam supported Co(OH)F and Co-P nanoarrays for energy-efficient hydrogen production: via urea electrolysis, J. Mater. Chem. A. 7 (2019) 3697–3703, doi:10.1039/c8ta10985k.
[26] M.S. Balogun, W. Qiu, W. Wang, P. Fang, X. Lu, Y. Tong, Recent advances in metal nitrides as high-performance electrode materials for energy storage devices, J. Mater. Chem. A. 3 (2015) 1364–1387, doi:10.1039/c4ta05565a.

[27] W.F. Chen, J.T. Muckerman, E. Fujita, Recent developments in transition metal carbides and nitrides as hydrogen evolution electrocatalysts, Chem. Commun. 49 (2013) 8896–8909, doi:10.1039/c3cc44076a.
[28] G. Fu, Z. Cui, Y. Chen, L. Xu, Y. Tang, J.B. Goodenough, Hierarchically mesoporous nickel-iron nitride as a cost-efficient and highly durable electrocatalyst for Zn-air battery, Nano Energy 39 (2017) 77–85, doi:10.1016/j.nanoen.2017.06.029.
[29] L. Xie, F. Qu, Z. Liu, X. Ren, S. Hao, R. Ge, G. Du, A.M. Asiri, X. Sun, L. Chen, In situ formation of a 3D core/shell structured Ni3N@Ni-Bi nanosheet array: an efficient non-noble-metal bifunctional electrocatalyst toward full water splitting under near-neutral conditions, J. Mater. Chem. A. 5 (2017) 7806–7810, doi:10.1039/c7ta02333b.
[30] L. He, J. Liu, Y. Liu, B. Cui, B. Hu, M. Wang, K. Tian, Y. Song, S. Wu, Z. Zhang, Z. Peng, M. Du, Titanium dioxide encapsulated carbon-nitride nanosheets derived from MXene and melamine-cyanuric acid composite as a multifunctional electrocatalyst for hydrogen and oxygen evolution reaction and oxygen reduction reaction, Appl. Catal. B Environ. 248 (2019) 366–379, doi:10.1016/j.apcatb.2019.02.033.
[31] D. Wu, Y. Wei, X. Ren, X. Ji, Y. Liu, X. Guo, Z. Liu, A.M. Asiri, Q. Wei, X. Sun, $Co(OH)_2$ nanoparticle-encapsulating conductive nanowires array: room-temperature electrochemical preparation for high-performance water oxidation electrocatalysis, Adv. Mater. (2018) 30, doi:10.1002/adma.201705366.
[32] A. Badruzzaman, A. Yuda, A. Ashok, A. Kumar, Recent advances in cobalt based heterogeneous catalysts for oxygen evolution reaction, Inorgan. Chim. Acta. (2020), doi:10.1016/j.ica.2020.119854.
[33] A. Yuda, A. Ashok, A. Kumar, A comprehensive and critical review on recent progress in anode catalyst for methanol oxidation reaction, Catal. Rev. - Sci. Eng. (2020), doi:10.1080/01614940.2020.1802811.
[34] W. Lu, T. Liu, L. Xie, C. Tang, D. Liu, S. Hao, F. Qu, G. Du, Y. Ma, A.M. Asiri, X. Sun, In situ derived Co-B nanoarray: a high-efficiency and durable 3D bifunctional electrocatalyst for overall alkaline water splitting, Small (2017) 13, doi:10.1002/smll.201700805.
[35] X. Xiong, Y. Ji, M. Xie, C. You, L. Yang, Z. Liu, A.M. Asiri, X. Sun, MnO_2-CoP_3 nanowires array: an efficient electrocatalyst for alkaline oxygen evolution reaction with enhanced activity, Electrochem. Commun. 86 (2018) 161–165, doi:10.1016/j.elecom.2017.12.008.
[36] R. Liu, D. Wu, X. Feng, K. Müllen, Nitrogen-doped ordered mesoporous graphitic arrays with high electrocatalytic activity for oxygen reduction, Angew. Chem. - Int. Ed. (2010), doi:10.1002/anie.200907289.
[37] S. Wang, D. Yu, L. Dai, D.W. Chang, J.B. Baek, Polyelectrolyte-functionalized graphene as metal-free electrocatalysts for oxygen reduction, ACS Nano (2011), doi:10.1021/nn200879h.
[38] L. Qu, Y. Liu, J.B. Baek, L. Dai, Nitrogen-doped graphene as efficient metal-free electrocatalyst for oxygen reduction in fuel cells, ACS Nano (2010), doi:10.1021/nn901850u.
[39] D. Dong, Z. Wu, J. Wang, G. Fu, Y. Tang, Recent progress in Co9S8-based materials for hydrogen and oxygen electrocatalysis, J. Mater. Chem. A. 7 (2019) 16068–16088, doi:10.1039/c9ta04972j.
[40] P. Ganesan, M. Prabu, J. Sanetuntikul, S. Shanmugam, Cobalt sulfide nanoparticles grown on nitrogen and sulfur codoped graphene oxide: an efficient electrocatalyst for oxygen reduction and evolution reactions, ACS Catal 5 (2015) 3625–3637, doi:10.1021/acscatal.5b00154.
[41] Y. Liu, C. Xiao, M. Lyu, Y. Lin, W. Cai, P. Huang, W. Tong, Y. Zou, Y. Xie, Ultrathin Co_3S_4 nanosheets that synergistically engineer spin states and exposed polyhedra that promote water oxidation under neutral conditions, Angew. Chem. - Int. Ed. 54 (2015) 11231–11235, doi:10.1002/anie.201505320.
[42] S. Huang, Y. Meng, S. He, A. Goswami, Q. Wu, J. Li, S. Tong, T. Asefa, M. Wu, N-, O-, and S-tridoped carbon-encapsulated Co_9S_8 nanomaterials: efficient bifunctional electrocatalysts for overall water splitting, Adv. Funct. Mater. (2017) 27, doi:10.1002/adfm.201606585.
[43] Y. Xu, Y. Hao, G. Zhang, X. Jin, L. Wang, Z. Lu, X. Sun, One-step scalable production of Co1−x S/graphene nanocomposite as high-performance bifunctional electrocatalyst, Part. Part. Syst. Charact. 33 (2016) 569–575, doi:10.1002/ppsc.201500242.
[44] Y. Wang, Y. Zhang, Y. Peng, H. Li, J. Li, B.J. Hwang, J. Zhao, Physical confinement and chemical adsorption of porous C/CNT micro/nano-spheres for CoS and Co 9 S 8 as advanced lithium batteries anodes, Electrochim. Acta. 299 (2019) 489–499, doi:10.1016/j.electacta.2018.11.138.
[45] J. Wang, H. Liu, Y. Liu, W. Wang, Q. Sun, X. Wang, X. Zhao, H. Hu, M. Wu, Sulfur bridges between Co_9S_8 nanoparticles and carbon nanotubes enabling robust oxygen electrocatalysis, Carbon N. Y. 144 (2019) 259–268, doi:10.1016/j.carbon.2018.12.031.
[46] H. Liu, F.X. Ma, C.Y. Xu, L. Yang, Y. Du, P.P. Wang, S. Yang, L. Zhen, Sulfurizing-induced hollowing of Co_9S_8 microplates with nanosheet units for highly efficient water oxidation, ACS Appl. Mater. Interfaces. 9 (2017) 11634–11641, doi:10.1021/acsami.7b00899.
[47] B.K. Barman, K.K. Nanda, A noble and single source precursor for the synthesis of metal-rich sulphides embedded in an N-doped carbon framework for highly active OER electrocatalysts, Dalt. Trans. 45 (2016) 6352–6356, doi:10.1039/c6dt00536e.
[48] X. Yuan, J. Yin, Z. Liu, X. Wang, C. Dong, W. Dong, M.S. Riaz, Z. Zhang, M.Y. Chen, F. Huang, Charge-transfer-promoted high oxygen evolution activity of $Co@Co_9S_8$ core-shell nanochains, ACS Appl. Mater. Interfaces. 10 (2018) 11565–11571, doi:10.1021/acsami.7b15890.
[49] L.L. Feng, G.D. Li, Y. Liu, Y. Wu, H. Chen, Y. Wang, Y.C. Zou, D. Wang, X. Zou, Carbon-armored Co_9S_8 nanoparticles as all-pH efficient and durable H2-evolving electrocatalysts, ACS Appl. Mater. Interfaces. 7 (2015) 980–988, doi:10.1021/am507811a.
[50] X. Zhou, X. Yang, M.N. Hedhili, H. Li, S. Min, J. Ming, K.W. Huang, W. Zhang, L.J. Li, Symmetrical synergy of hybrid Co_9S_8-MoSx electrocatalysts for hydrogen evolution reaction, Nano Energy 32 (2017) 470–478, doi:10.1016/j.nanoen.2017.01.011.
[51] L. Gu, H. Zhu, D.N. Yu, S.G. Zhang, J. Chen, J. Wang, M. Wan, M. Zhang, M.L. Du, A facile strategy to synthesize cobalt-based self-supported material for electrocatalytic water splitting, Part. Part. Syst. Charact. (2017) 34, doi:10.1002/ppsc.201700189.
[52] R. Liu, H. Zhang, X. Zhang, T. Wu, H. Zhao, G. Wang, Co_9S_8@N,P-doped porous carbon electrocatalyst using biomass-derived carbon nanodots as a precursor for overall water splitting in alkaline media, RSC Adv 7 (2017) 19181–19188, doi:10.1039/c7ra01798g.
[53] J. Masud, A.T. Swesi, W.P.R. Liyanage, M. Nath, Cobalt selenide nanostructures: an efficient bifunctional catalyst with high current density at low coverage, ACS Appl. Mater. Interfaces. (2016), doi:10.1021/acsami.6b04862.
[54] X. Cao, Y. Hong, N. Zhang, Q. Chen, J. Masud, M.A. Zaeem, M. Nath, Phase exploration and identification of multinary transition-metal selenides as high-efficiency oxygen evolution electrocatalysts through combinatorial electrodeposition, ACS Catal. (2018), doi:10.1021/acscatal.8b01977.
[55] X. Yu, M. Zhang, W. Yuan, G. Shi, A high-performance three-dimensional Ni-Fe layered double hydroxide/graphene electrode for water oxidation, J. Mater. Chem. A. (2015), doi:10.1039/c5ta01034a.
[56] J. Zhang, J. Chen, Y. Jiang, F. Zhou, G. Wang, R. Wang, Tungsten carbide encapsulated in nitrogen-doped carbon with iron/cobalt carbides electrocatalyst for oxygen reduction reaction, Appl. Surf. Sci. 389 (2016) 157–164, doi:10.1016/j.apsusc.2016.07.071.
[57] D. Zhao, J. Zhang, C. Fu, J. Huang, D. Xiao, M.M.F. Yuen, C. Niu, Enhanced cycling stability of ring-shaped phosphorus inside multi-walled carbon nanotubes as anodes for lithium-ion batteries, J. Mater. Chem. A. 6 (2018) 2540–2548, doi:10.1039/c7ta07683e.
[58] K.P. De Jong, J.W. Geus, Carbon nanofibers: catalytic synthesis and applications, Catal. Rev. - Sci. Eng. (2000), doi:10.1081/CR-100101954.
[59] M. Terrones, W.K. Hsu, A. Schilder, H. Terrones, N. Grobert, J.P. Hare, Y.Q. Zhu, M. Schwoerer, K. Prassides, H.W. Kroto, D.R.M. Walton, Novel nanotubes and encapsulated nanowires, Appl. Phys. A Mater. Sci. Process. 66 (1998) 307–317, doi:10.1007/s003390050671.
[60] S. Fan, M.G. Chapline, N.R. Franklin, T.W. Tombler, A.M. Cassell, H. Dai, Self-oriented regular arrays of carbon nanotubes and their field emission properties, Science (80-.). 283 (1999) 512–514. https://doi.org/ 10.1126/science.283.5401.512.
[61] N.I. Maksimova, O.P. Krivoruchko, G. Mestl, V.I. Zaikovskii, A.L. Chuvilin, A.N. Salanov, E.B. Burgina, Catalytic synthesis of carbon nanostructures from polymer precursors, J. Mol. Catal. A Chem. (2000) 301–307, doi:10.1016/S1381-1169(00)00095-9.
[62] S. Ghosh, S. Ramaprabhu, Green synthesis of transition metal nanocrystals encapsulated into nitrogen-doped carbon nanotubes for efficient carbon dioxide capture, Carbon N. Y. 141 (2019) 692–703, doi:10.1016/j.carbon.2018.09.083.
[63] L. Chen, D. Huang, S. Ren, T. Dong, Y. Chi, G. Chen, Preparation of graphite-like carbon nitride nanoflake film with strong fluorescent and electrochemiluminescent activity, Nanoscale 5 (2013) 225–230, doi:10.1039/c2nr32248j.
[64] M. Groenewolt, M. Antonietti, Synthesis of g-C_3N_4 nanoparticles in mesoporous silica host matrices, Adv. Mater. 17 (2005) 1789–1792, doi:10.1002/adma.200401756.
[65] M. Deifallah, P.F. McMillan, F. Corà, Electronic and structural properties of two-dimensional carbon nitride graphenes, J. Phys. Chem. C. 112 (2008) 5447–5453, doi:10.1021/jp711483t.
[66] C. Ehrhardt, M. Gjikaj, W. Brockner, Thermal decomposition of cobalt nitrato compounds: preparation of anhydrous cobalt(II)nitrate and its characterisation by Infrared and Raman spectra, Thermochim. Acta. 432 (2005) 36–40, doi:10.1016/j.tca.2005.04.010.
[67] X. Dai, Z. Li, Y. Ma, M. Liu, K. Du, H. Su, H. Zhuo, L. Yu, H. Sun, X. Zhang, Metallic cobalt encapsulated in bamboo-like and nitrogen-rich carbonitride nanotubes for hydrogen evolution reaction, ACS Appl. Mater. Interfaces. 8 (2016) 6439–6448, doi:10.1021/acsami.5b11717.
[68] A. Leonhardt, S. Hampel, C. Müller, I. Mönch, R. Koseva, M. Ritschel, D. Elefant, K. Biedermann, B. Büchner, Synthesis, properties, and applications of ferromagnetic-filled carbon nanotubes, Chem. Vap. Depos. 12 (2006) 380–387, doi:10.1002/cvde.200506441.
[69] H.U.R. Memon, A. Williams, P.T. Williams, Shock tube pyrolysis of thiophene, Int. J. Energy Res. 27 (2003) 225–239, doi:10.1002/er.870.
[70] S. Esconjauregui, C.M. Whelan, K. Maex, The reasons why metals catalyze the nucleation and growth of carbon nanotubes and other carbon nanomorphologies, Carbon N. Y. 47 (2009) 659–669, doi:10.1016/j.carbon.2008.10.047.
[71] G. Du, W. Li, Y. Liu, Filling carbon nanotubes with Co9S8 nanowires through in situ catalyst transition and extrusion, J. Phys. Chem. C. 112 (2008) 1890–1895, doi:10.1021/jp710543u.
[72] N. Demoncy, O. Stéphan, N. Brun, C. Colliex, A. Loiseau, H. Pascard, Filling carbon nanotubes with metals by the arc-discharge method: the key role of sulfur, Eur. Phys. J. B. 4 (1998) 147–157, doi:10.1007/s100510050363.
[73] M. Lin, J.P.Y. Tan, C. Boothroyd, K.P. Loh, E.S. Tok, Y.L. Foo, Dynamical observation of bamboo-like carbon nanotube growth, Nano Lett 7 (2007) 2234–2238, doi:10.1021/nl070681x.

[74] L.S. Lobo, S.A.C. Carabineiro, Explaining bamboo-like carbon fiber growth mechanism: catalyst shape adjustments above tammann temperature, C — J. Carbon Res (2020), doi:10.3390/c6020018.
[75] V.I. Zaikovskii, V.V. Chesnokov, R.A. Buyanov, The relationship between the state of active species in a Ni/Al_2O_3 catalyst and the mechanism of growth of filamentous carbon, Kinet. Catal. (2001), doi:10.1023/A:1013235300777.
[76] R. Sharma, P. Rez, M. Brown, G. Du, M.M.J. Treacy, Dynamic observations of the effect of pressure and temperature conditions on the selective synthesis of carbon nanotubes, Nanotechnology (2007), doi:10.1088/0957-4484/18/12/125602.
[77] Z. Yu, D. Chen, B. Tøtdal, A. Holmen, Effect of support and reactant on the yield and structure of carbon growth by chemical vapor deposition, J. Phys. Chem. B. (2005), doi:10.1021/jp0449760.
[78] S. Hofmann, R. Sharma, C. Ducati, G. Du, C. Mattevi, C. Cepek, M. Cantoro, S. Pisana, A. Parvez, F. Cervantes-Sodi, A.C. Ferrari, R. Dunin-Borkowski, S. Lizzit, L. Petaccia, A. Goldoni, J. Robertson, In situ observations of catalyst dynamics during surface-bound carbon nanotube nucleation, Nano Lett (2007), doi:10.1021/nl0624824.
[79] L.L. Feng, M. Fan, Y. Wu, Y. Liu, G.D. Li, H. Chen, W. Chen, D. Wang, X. Zou, Metallic Co_9S_8 nanosheets grown on carbon cloth as efficient binder-free electrocatalysts for the hydrogen evolution reaction in neutral media, J. Mater. Chem. A. 4 (2016) 6860–6867, doi:10.1039/c5ta08611f.
[80] J. Bao, X. Zhang, B. Fan, J. Zhang, M. Zhou, W. Yang, X. Hu, H. Wang, B. Pan, Y. Xie, Ultrathin spinel-structured nanosheets rich in oxygen deficiencies for enhanced electrocatalytic water oxidation, Angew. Chem. - Int. Ed. 54 (2015) 7399–7404, doi:10.1002/anie.201502226.
[81] P. Li, M. Wang, X. Duan, L. Zheng, X. Cheng, Y. Zhang, Y. Kuang, Y. Li, Q. Ma, Z. Feng, W. Liu, X. Sun, Boosting oxygen evolution of single-atomic ruthenium through electronic coupling with cobalt-iron layered double hydroxides, Nat. Commun. (2019) 10, doi:10.1038/s41467-019-09666-0.
[82] Y. Dong, H. Pang, H. Bin Yang, C. Guo, J. Shao, Y. Chi, C.M. Li, T. Yu, Carbon-based dots co-doped with nitrogen and sulfur for high quantum yield and excitation-independent emission, Angew. Chem. - Int. Ed. 52 (2013) 7800–7804, doi:10.1002/anie.201301114.
[83] C. Li, X. Han, F. Cheng, Y. Hu, C. Chen, J. Chen, Phase and composition controllable synthesis of cobalt manganese spinel nanoparticles towards efficient oxygen electrocatalysis, Nat. Commun. 6 (2015), doi:10.1038/ncomms8345.
[84] X. Han, X. Wu, C. Zhong, Y. Deng, N. Zhao, W. Hu, $NiCo_2S_4$ nanocrystals anchored on nitrogen-doped carbon nanotubes as a highly efficient bifunctional electrocatalyst for rechargeable zinc-air batteries, Nano Energy (2017), doi:10.1016/j.nanoen.2016.12.008.
[85] S. Chen, Y. Cheng, G. Zhang, Y.W. Zhang, Spontaneous directional motion of water molecules in single-walled carbon nanotubes with a stiffness gradient, Nanoscale Adv. (2019), doi:10.1039/c8na00322j.
[86] X. Li, Y. Shi, Y. Yang, H. Du, R. Zhou, Y. Zhao, How does water-nanotube interaction influence water flow through the nanochannel, J. Chem. Phys. (2012), doi:10.1063/1.4707346.
[87] J. Zou, B. Ji, X.Q. Feng, H. Gao, Self-assembly of single-walled carbon nanotubes into multi walled carbon nanotubes in water: molecular dynamics simulations, Nano Lett. (2006), doi:10.1021/nl052289u.
[88] Z. Cui, D. Li, B. Ji, Effect of curvature on the behaviors of confined water layers, Int. J. Appl. Mech. (2015), doi:10.1142/S1758825115500842.
[89] T. Shinagawa, M.T.K. Ng, K. Takanabe, Electrolyte engineering towards efficient water splitting at Mild pH, ChemSusChem. (2017), doi:10.1002/cssc.201701266.
[90] M. Tavakkoli, T. Kallio, O. Reynaud, A.G. Nasibulin, J. Sainio, H. Jiang, E.I. Kauppinen, K. Laasonen, Maghemite nanoparticles decorated on carbon nanotubes as efficient electrocatalysts for the oxygen evolution reaction, J. Mater. Chem. A. (2016), doi:10.1039/c6ta01472k.
[91] A. Ashok, A. Kumar, J. Ponraj, S.A. Mansour, Synthesis and growth mechanism of bamboo like N-doped CNT/Graphene nanostructure incorporated with hybrid metal nanoparticles for overall water splitting, Carbon N. Y. (2020), doi:10.1016/j.carbon.2020.08.047.
[92] Z. Luo, S. Lim, Z. Tian, J. Shang, L. Lai, B. MacDonald, C. Fu, Z. Shen, T. Yu, J. Lin, Pyridinic N doped graphene: synthesis, electronic structure, and electrocatalytic property, J. Mater. Chem. 21 (2011) 8038–8044, doi:10.1039/c1jm10845j.
[93] J.O. Hwang, J.S. Park, D.S. Choi, J.Y. Kim, S.H. Lee, K.E. Lee, Y.H. Kim, M.H. Song, S. Yoo, S.O. Kim, Workfunction-tunable, N-doped reduced graphene transparent electrodes for high-performance polymer light-emitting diodes, ACS Nano 6 (2012) 159–167, doi:10.1021/nn203176u.
[94] Y. Zhu, L. Zhang, B. Zhao, H. Chen, X. Liu, R. Zhao, X. Wang, J. Liu, Y. Chen, M. Liu, Improving the activity for oxygen evolution reaction by tailoring oxygen defects in double perovskite oxides, Adv. Funct. Mater. 29 (2019), doi:10.1002/adfm.201901783.
[95] Y. Zhu, X. Liu, S. Jin, H. Chen, W. Lee, M. Liu, Y. Chen, Anionic defect engineering of transition metal oxides for oxygen reduction and evolution reactions, J. Mater. Chem. A. (2019), doi:10.1039/c8ta12477a.